A historical perspective on porphyrin-based metal–organic frameworks and their applications

Xuan Zhang[a], Megan C. Wasson[a], Mohsen Shayan[d], Ellan K. Berdichevsky[d], Joseph Ricardo-Noordberg[e], Zujhar Singh[e], Edgar K. Papazyan[f], Anthony J. Castro[f], Paola Marino[e], Zvart Ajoyan[e], Zhijie Chen[a], Timur Islamoglu[a], Ashlee J. Howarth[e,*], Yangyang Liu[f,*], Marek B. Majewski[e,*], Michael J. Katz[d,*], Joseph E. Mondloch[c,*], Omar K. Farha[a,b,*]

[a]Department of Chemistry and International Institute for Nanotechnology, Northwestern University, Evanston, IL 60208, United States

[b]Department of Chemical and Biological Engineering, Northwestern University, 2145 Sheridan Road, Evanston, IL 60208, United States

[c]Department of Chemistry, University of Wisconsin-Stevens Point, 2100 Main Street, Stevens Point, WI 54481, United States

[d]Department of Chemistry, Memorial University of Newfoundland, 230 Elizabeth Avenue, St. John's, Newfoundland and Labrador, A1C 5S7, Canada

[e]Department of Chemistry and Biochemistry and Centre for NanoScience Research, Concordia University, 7141 Sherbrooke St. W., Montréal, Québec, H4B 1R6, Canada

[f]Department of Chemistry and Biochemistry, California State University, Los Angeles, 5151 State University Drive, Los Angeles, CA 90032, United States

Abstract

Porphyrins are important molecules widely found in nature in the form of enzyme active sites and visible light absorption units. Recent interest in using these functional molecules as building blocks for the construction of metal–organic frameworks (MOFs) have rapidly increased due to the ease in which the locations of, and the distances between, the porphyrin units can be controlled in these porous crystalline materials. Porphyrin-based MOFs with atomically precise structures provide an ideal platform for the investigation of their structure–function relationships in the solid state without compromising accessibility to the inherent properties of the porphyrin building blocks. This review will provide a historical overview of the development and applications of porphyrin-based MOFs from early studies focused on design and structures, to recent efforts on their utilization in biomimetic catalysis, photocatalysis, electrocatalysis, sensing, and biomedical applications.

*Corresponding authors. ashlee.howarth@concordia.ca (A.J. Howarth), yliu114@calstatela.edu (Y. Liu), marek.majewski@concordia.ca (M.B. Majewski), michael.jacob.katz@gmail.com (M.J. Katz), mojo0001@gmail.com (J.E. Mondloch), o-farha@northwestern.edu (O.K. Farha).

Keywords

Porphyrin; Metal–organic frameworks; Catalysis; Sensing; Biomedical applications

1. Introduction

Metal–organic frameworks (MOFs) are crystalline porous materials comprising highly versatile functional inorganic and organic building blocks, which have enabled their widespread utilization in gas storage and separation [1,2], catalysis [3,4], water remediation [5,6], biomolecule encapsulation [7,8], sensing [9,10], electronics and so on [11–13]. The metal-based ions/clusters and the organic linkers of MOFs are highly tunable in the sense of their geometry, connectivity and functionality for the construction of MOFs with different structures and functionalities [14–16]. Among the different families of functional organic linkers that have been employed in synthesizing MOFs, porphyrin-based linkers have garnered special attention owing to their unique geometry and versatile functionality for a variety of applications such as biomimetic catalysis, electrocatalysis, photocatalysis, sensing and biomedical applications [17–21].

Porphyrins are a class of N-heterocycles widely found in nature in the form of hemoglobins in animal blood for carrying oxygen, chlorophylls in green plants for photosynthesis, catalase for the decomposition of hydrogen peroxide, cytochromes for a variety of oxidative reactions, vitamin B_{12} for cell metabolism and so on [22,23]. While porphyrins as functional molecules are usually employed in homogeneous systems, the heterogenization of these moieties in crystalline frameworks with long-range-ordered structures will help facilitate their recyclability, and more importantly, understand their structure–property relationships. In this vein, MOFs with porphyrin-based struts are ideal candidates for arranging them in a porous framework with precise structures while maintaining the accessibility of the porphyrin species to different substrates. As such, there have been increasing interests over the past two decades in the structural and functional study of porphyrin-based MOFs for their unique and versatile applications, as suggested by the fast-increasing number of reports in the literature and structures in the Cambridge Structural Database (CSD) (Fig. 1) [24,25].

Herein, we provide a historical overview of the development and applications of porphyrin-based MOFs. Following a synopsis of the design of porphyrin-based MOFs, the utilization of these MOFs in biomimetic catalysis, photocatalysis, electrocatalysis, sensing, and biomedical applications will be highlighted; and promising future directions and interests in porphyrin-based MOFs will be discussed. This review will focus on examples of MOFs with the porphyrin moiety as a building block wherein precise structures can be determined.

2. Synthesis and Design of Porphyrin-Based MOFs

From a historical point of view, the development of porphyrin-based MOFs has followed the general trend of MOF development as guided by the principles of reticular chemistry [26,27]. During the early development of porphyrin-based porous coordination polymers, coordination bonds between metal nodes and neutral organic linkers often gave frameworks that were prone to collapse after guest solvent removal. For example, in 1994, Robson

reported coordination network structures containing Cu(II) ions and neutral pyridyl- or cyanophenyl-substituted porphyrin building blocks [28]. While the structures exhibited large channels occupied by solvent molecules and counter anions, amorphization incurred upon the loss of solvent molecules. After that, a few more examples of coordination frameworks based on metal-pyridylporphyrin linkages were reported where structural analysis indicated potential void space in the frameworks [29–32].

Early examples of porphyrin-based framework materials with metal-carboxylate coordination bonds consisted of Zn(II)/Na(I) ions and a tetra(4-carboxyphenyl)porphyrin (TCPP), as demonstrated by Goldberg [33,34]. In 2002, Suslick reported a microporous framework, PIZA-1 (PIZA = porphyrinic Illinois zeolite analogue) that was constructed from strong metal-charged carboxylateporphyrin bonds [35]. PIZA-1 consisted of linear trinuclear Co-based nodes and TCPP linkers, which gave rise to high structural robustness and microporosity with a BET area of 125 m^2/g, as evidenced by N_2 and solvent vapor adsorption studies. Subsequently, PIZA-4, with a $[Zn4O]^{6+}$ metal node—similar to that of MOF-5—and the TCPP linker was reported with a Langmuir surface area of 800 m^2/g [36].

Most of these early studies of porphyrin-based framework materials focused on structural explorations [34,37], with the only example of catalytic activity reported in PIZA-3 [38]. Since 2009, the numbers of research reports on porphyrin-based MOFs have been steadily increasing (Fig. 1). For example, Nguyen, Hupp and Farha reported permanent porosity in a series of pillared porphyrin (*i.e.,* (5,15-dipyridyl-10,20-bis(pentafluorophenyl))porphyrin (H_2-DPBPP)) MOFs, and the accessibility of their catalytically active porphyrin units were demonstrated in a variety of applications such as acyl-transfer catalysis, oxidative catalysis, and light harvesting [39–41].

Toward the goal of practical applications, the synthesis of MOFs—including porphyrin-based ones—with enhanced thermal, chemical and mechanical stabilities has been a major thrust [42]. In 2012, Rosseinsky reported a water stable porphyrinic MOF based on $Al(OH)O_4$ rod packing secondary building units (SBUs) and TCPP [43]. Since the report of the first Zr-based MOFs, this family of MOFs have been widely investigated due to their high stability and versatile structures [44,45]. Some examples of porphyrin-based Zr-MOFs are PCN-222/MOF-545 [46,47], PCN-223 [48], NU-902 [49], MOF-525 [47], PCN-224 [50], PCN-225 [51], PCN-138 [52] and PCN-226 [53]. Constructed from the same building blocks of Zr_6 clusters and TCPP linkers, these MOFs exhibited high structural and topological diversity owing to the variable connectivity of the Zr_6 node and rotation angles of the phenyl arms of the TCPP linkers. In addition, PCN-600 [54] and other trigonal planar trinuclear node-based porphyrinic MOFs have shown highly versatile node-metal variations in addition to their high stability [55]. Besides metal-carboxylate linkages, porphyrin MOFs based on metal-azolate coordination bonds have been explored. For example, tetrazolyl- or pyrazolyl-substituted porphyrins have been employed to construct MOFs that can withstand basic conditions [56,57].

Even though the intrinsic square planar geometry of the porphine core limits geometries of the porphyrin linkers, systematic variations of the backbone yields a diverse group of porphyrin-based organic linkers with different geometries and connectivity for MOF

designs. Besides the most widely used tetratopic TCPP, ditopic bicarboxylate-substituted porphyrin linkers like 5,15-bis(4-carboxyphenyl)porphyrin (H_2BCPP) have been developed for the synthesis of MOFs [58–60]. Moreover, Ma and coworkers employed a less symmetric tritopic porphyrinoid linker (5,10,15-t ris(p-carboxylphenyl)corrole (H_3TCPC)) to form Corrole-MOF-1 with rare 9-connected Zr_6 nodes [61]. Li utilized a mixed bipyridyl-bicarboxylate-substituted porphyrin linker, DCDPP (H_2-DCDPP = 5,15-di(4-carboxylphenyl)-10,20-di(4-pyridyl)porphyrin), to yield BUT-83 with cobalt nodes; this framework demonstrated proton conducting properties [62]. In addition, tetratopic linkers (H_4BDCPP, Fig. 2) with di-substituted porphyrin and octatopic linkers with tetra-substituted porphyrin (H_8TDCPP, Fig. 2) formed MOFs with distinct structures [63–65].

3. Porphyrin-Based MOFs as Biomimetics of Cytochrome P450

P450 belongs to a group of peroxidase enzymes existing in nature which catalyze the oxidation of a wide range of organic molecules including the monooxygenation of C—H and C=C bonds, C—C bond formation, C—C bond cleavage, and Baeyer–Villiger oxidation [66]. The active site of all these enzymes feature similar iron porphyrinic compounds with subtle differences in the proximal and distal positions. Specifically, the active site of P450 contains a heme-Fe(III) with one axial site of the Fe(III) center coordinated to a cysteine residue (Cys 400) anchoring the assembly to the peptide chain. The vacant second axial coordination site subsequently facilitates the binding of O_2 and reactants to the metal center and hence plays a highly important role in catalytic reactions involving P450. Moreover, a highly electrophilic tetravalent $(P)Fe(IV)O^{\bullet+}$ radical cation further promotes binding of the active center with substrate molecules, resulting in the addition of a single oxygen atom (Fig. 3) [67]. Taken together, these features of the peroxidase enzymes have motivated researchers to mimic the active site [66,68–72] for a wide breadth of applications.

Designing synthetic scaffolds to emulate the microenvironments found in an enzyme active site that offer high catalytic activity and substrate selectivity remains a sought-after goal. To mimic P450 activity, as well as to drive these transformations heterogeneously, porphyrin-based MOFs have emerged as one of the champion candidates. Porphyrin MOFs with different metalation are synthetically accessible through the use of appropriate metalloporphyrin linkers during synthesis [46,63,73–77] or postsynthetically by cation exchange into metal free porphyrin linkers [77,78]. Through their periodic arrangement as MOF structural linkers, spatially isolated porphyrin entities enable heightened substrate access to single catalytic sites. Thus, a library of porphyrin-based MOFs displaying similar reactivity to P450 exists in literature, encompassing different catalytic environments and capable of a variety of catalytic transformations (including oxidation catalysis) mimicking natural cytochrome P450.

Seminal work in porphyrin-based MOFs first utilized Zr-based nodes in conjunction with iron-metallated porphyrin linkers. Morris *et al.* and Feng *et al.* simultaneously reported a stable Zr-MOF known as PCN-222(Fe) and MOF-545, respectively, composed of highly stable Zr_6 cluster nodes and Fe-TCPP [TCPP = tetrakis(4-car boxyphenyl)-porphyrin] as the organic linker mimicking the heme-like active site (Fig. 4) [46,47]. The exceptional stability of PCN-222(Fe) in water and even in concentrated acids combined with large 1D pores of up

to 37 Å in diameter positioned this MOF as a suitable candidate for use in peroxidase biomimetic heterogeneous catalysis. PCN-222(Fe) was active in oxidizing substrates such as pyrogallol (Table 1 Entry 1), 3,3,5,5-tetramethylbenzidine, and *o*-phenylenediamine with excellent substrate binding affinity ($K_m = 0.33$, 1.63, 8.92 mM, respectively) and catalytic activity ($k_{cat} = 16.1$, 14.0, 7.3 min^{-1}, respectively). The better performance of PCN-222(Fe) than hemin in aqueous media was attributed to the isolated porphyrin species in the highly porous framework.

By adjusting the reaction conditions and/or the identity of the organic linker used, the coordination environment around the Zr_6 cluster in MOFs can be tuned [79]. Leveraging this property, Feng *et al.* carefully varied the starting ratio of a Zr_6 cluster node and TCPP heme-like ligand to construct a series of highly stable MOFs, PCN-224 (M = none, Ni, Co, Fe) [50]. The PCN-224 family consists of the same Zr_6 nodes within PCN-222, but the nodes are 6-connected (PCN-224) instead of 8-connected (PCN-222). PCN-224(Co) acted as a highly efficient catalyst for the coupling of CO_2 and epoxide (Fig. 5 and Table 1 Entry 2). The Co-based MOF catalyst achieved 42% conversion efficiency and preserved this activity over three consecutive cycles (39%).

Variations in node connectivity and symmetry can access many topologies when using the TCPP linker and Zr_6 nodes. With the use of a kinetically controlled synthetic process, Feng *et al.* reported the first example of a **shp-a** network in a porphyrinic Zr-MOF (PCN-223); this belonged to one of the three edge-transitive (4,12)-c nets predicted by Delgado-Friedrichs, O'Keeffe and Yaghi [48,80]. The framework of PCN-223 contains 12-connected Zr_6 cluster nodes and rare D_{6h} symmetry. A coordinatively unsaturated cationic iron(III) porphyrin center in PCN-223(Fe) heterogeneously catalyzed the hetero-Diels – Alder (hDA) reaction between a diene and traditionally unreactive aldehydes (Table 1 Entry 3) in 98% yield and preserving 90% conversion even after five cycles.

Using a node preassembly strategy, Wang *et al.* obtained a new iron-based MOF, PCN-600, with **stp-a** topology featuring the coordination of TCPP to six-connected $Fe_3O(COO^-)_6OH$ nodes [54]. PCN-600 exhibited 31 A wide 1D channels and 1.80 cm^3 g^{-1} of pore volume. PCN-600(Fe) was employed as a peroxidase mimic to catalyze a co-oxidation reaction (Table 1 Entry 4). Kinetic studies revealed a smaller K_m value of the MOF (6.37 mM) as compared to that of cytochrome *c* itself (89.4 mM), indicating a higher affinity of the former for the substrate, which was attributed to the well-isolated accessible active sites and the confinement effect of the MOF.

The preparation of Fe-based porphyrinic MOFs involves a relatively high degree of synthetic complexity; some cases require node preassembly or the use of inorganic/organic bases which promote coordination of the metal center in the porphyrin linker to yield the desired framework. To circumvent such intricacies, Liu *et al.* reported a one pot, three-component modulator (pair of carboxylic acids and water) synthetic approach to yield $[Fe(OH)O_4]_n^{6+}$ chains, giving M–PMOF–3(Fe) (M = Fe, Co, Ni, Cu) with **fry**-topology [81]. This MOF demonstrated stability in a wide scope of conditions including 2 M HCl for two days, an overall pH range from 0 to 11, many common organic solvents for seven days, and thermal integrity up to 350 °C. Subsequently, the authors interrogated this family of MOFs in the

performance of P450-like reactions with the use of atmospheric oxygen to oxidize inert C–H bonds. When investigating Fe-PMOF-3(Fe) and Cu-PMOF-3(Fe) respectively in the presence of N-hydroxyphthalimide (NHPI), the aerobic oxidation of ethylbenzene in air yielded acetophenone (Table 1 Entry 5) in 61% and 82% yields after 24 h with a ketone:alcohol selectivity of up to 98:2 (under an extended reaction period).

Beyzavi and co-workers synthesized an Fe-porphyrin modified version of Hf-NU-1000 whose framework is structurally similar to PCN-222 [82]. The Hf_6 cluster is eight-connected with Fe-TCPP ligands giving rise to ca. 35 Å hexagonal and 12 Å triangular channels. The authors treated the synthesized material with anhydrous $FeCl_3$ to ensure that every porphyrin linker was metalated with Fe^{3+} ions. This treatment not only increased the Fe:Hf ratio, but also removed any additional ligated benzoic acid modulator molecules due to *in situ* generation of HCl, hence increasing the BET area from 1440 to 1600 m^2/g. Owing to cooperativity between the metalated porphyrin and Fe found on the node post $FeCl_3$ treatment, this MOF facilitated a tandem catalytic reaction to regioselectively catalyze the reaction of styrene to 1,2-aminoalcohol (Fig. 6). This kinetically favored product motif is found in biologically relevant molecules such as in β-blockers instead of the thermodynamically favored 1,2-hydroxyl amine (Table 1 entry 6) Fig. 7.

Multifunctional rare-earth (RE) metals display distinctive properties as compared to d-block transition metals. Therefore, using RE-metal clusters as MOF nodes results in unprecedented architectures and many favorable optical [83], catalytic [84,85], separation [86], and adsorption[87] properties. Du *et al.* reported a series of stable highly connected RE-cluster-based MOF, NUPF-2 M (M = Y, Gd, Tb, Dy, Er, Yb) synthesized *via* both solvothermal and microwave approaches, which demonstrated permanent porosity along with chemical and thermal stabilities through solvothermal as well as microwave syntheses[88]. Four-connected TCPP linkers in conjunction with 12-connected nonanuclear Y(III) clusters form NUPF-2Y. Moreover, the postsynthetic metallation of prism-shaped crystals of NUPF-2Y with $FeCl_3$ resulted in NUPF-2Y-FeCl competent for N–H carbene insertion (Table 1 entry 7) with a catalytic yield of 92% after an impressive four reaction cycles.

Among the oxidation processes, porphyrin MOFs have been particularly effective for the generation of epoxides, which are highly valuable synthetic chemicals. While MOFs with Fe-porphyrin sites serve as an obvious catalyst candidate, given that they most closely resemble P450, the use of other transition metals allows for a greater diversity of reactivity. Thus, research teams explored other transition metals studied for the epoxidation of olefins using metalloporphyrin MOFs, including, manganese [74,75,89–91], palladium [75], cobalt [92,93], cadmium [93], and nickel [94]. In some cases, molecular oxygen served as the oxidant [90,95], allowing for the cheaper manufacturing of desired epoxides as compared to other methods.

Meng *et al.* reported a metal-metalloporphyrin framework (MMPF) based on **fcu**-MOF-1 and prepared from 5,15-bis(3,5-dicarboxyphenyl)-10,20-bis(2,6-dibromophenyl)porphyrin (dcdbp) and $Co(NO_3)_2$ [94]. The Co-porphyrin MOF, MMPF-3, with a BET area of 750 m^2/g, catalyzed the epoxidation of *trans*-stilbene with a 95.7% conversion and an 87.1% selectivity toward the epoxide using *tert*-butyl hydroperoxide (TBHP, Table 1 entry 8).

MMPF-3 showed a greater conversion than both the **fcu**-MOF-1 and the homogeneous controls, demonstrating the necessity for both an open Co-porphyrin catalytic site and the high porosity of the MOF. The authors attributed the greater catalytic activity of MMPF-3 as compared to **fcu**-MOF-1 to the additional active cobalt centers in the metallated linkers of MMPF-3. An absence of cobalt leaching in the reaction solution and comparable conversion and selectivity after eight cycles illustrated the heterogeneity of the MOF catalyst [92]. To study the effects of electron withdrawing and electron donating groups present on a series of conjugated olefins, Zhang *et al.* studied the epoxidation of styrene derivatives *via* a Ni-porphyrin MOF synthesized using a TCPP ligand and $NiCl_2$, MMPF-20 (Table 1 entry 9). The authors observed that electron withdrawing groups reduced the yield of epoxide, while electron donating groups and increased conjugation increased the yields.

In addition to epoxidations, metalloporphyrin MOFs have been used to catalyze other oxidation reactions such as those of alkylbenzene [63,96], cyclohexane [73,75], fullerene [97], and catechol [95] as well as alkyne hydration [78]. Yang *et al.* reported the use of three metalloporphyrin MOFs for the oxidation of alkylbenzenes to ketones. The MOFs contain a metalated 5,10,15,20-tetrakis(3,5-biscarboxyphenyl)porphyrin (M–OCPP) linker, yet differ in metallic cluster identity and/or metallic species in the porphyrin linker. Specifically, ZJU-18 features Mn-porphyrin linkers with Mn cluster nodes, while ZJU-19 possesses the same Mn cluster nodes but Ni-porphyrin linkers instead. Lastly, Mn-porphyrin linkers with Cd cluster nodes comprise ZJU-20. The authors investigated a library of alkyl benzenes and reported the highest yield for ethylbenzene oxidation to acetophenone using ZJU-18 as the catalyst with > 99% conversion and > 99% selectivity (Table 1 entry 10), again surpassing the efficiency of the homogeneous catalyst (MnCl-Me_8OCPP). However, with larger substrates, a reduction in catalytic activity occurred for ZJU-18. Its pore window diameter of 11.5 Å likely precluded the diffusion of larger molecules into the MOF to access the active sites. Furthermore, ZJU-19 (with Mn-node and Ni-porphyrin linker) and ZJU-20 (with Cd-node and Mn-porphyrin linker) illustrated decreased catalytic activity versus ZJU-18, suggesting the possible cooperativity between Mn-node and Mn-porphyrin linker in the catalytic performance of the MOF [63]. Zhao and Wu further expanded this work through the addition of a polyoxometalate (POM) as a cocatalyst to CZJ-6, a copper metalloporphyrinic framework with Cu nodes, which performed better than either CJZ-6 or POM catalysts on their own [96]. With this work, POMs served as electron reservoirs to enable the activation of molecular oxygen directly.

Beyond adding cooperative guest interactions, the proximity of active centers can facilitate cooperative catalysis. In one interesting example, Lin *et al.* reported a metalloporphyrin MOF with TCPP as the linker and $[In(COO^-)_4]^-$ nodes, that form a twofold interpenetrated framework [78]. Further treatment with Co(III) ions yielded In-Co(TBP)-MOF or Co(TBP)-MOF, featuring the two metals within ~ 8.8 Å of each other due to the framework catenation and thus allowing for cooperative catalysis (Scheme 1). With this platform, the authors studied their efficacy for the catalytic hydration of alkynes to form carbonyl derivatives. In-Co(TBP)-MOF, despite having a relatively low BET area of 190 m^2/g, achieved a 100% conversion of phenylacetylene to acetophenone with 0.1 mol% loading (Table 1 entry 11) while the homogeneous controls resulted in < 25% conversions after 20 h. Even a 0.01 mol

% loading displayed 92% conversion after seven days. Catalytic activity was maintained after recycling the catalyst six times.

In addition to oxidation reactions, researchers investigated the catalytic performance of metalloporphyrin MOFs for Aldol condensations [74,75], Diels-Alder reactions [97], C–H bond halogenations [76], CO_2 fixation by cycloaddition into epoxides [50,60,77,91,98–100] or aziridines [101], –OH insertion [102], acyl transfer [49,103], and asymmetric cyanosilation of carbonyl compounds [95]. With the great variety of reactions and the porous nature of MOFs, further opportunities include accomplishing sequential reactions with a single MOF catalyst with different metal centers [91] or even anchoring a second catalyst[104] or co-catalyst [96].

To create an orthogonal tandem catalytic system, Beyzavi *et al.* reported a MOF thin film featuring two linkers: a Mn-porphyrin carboxylate linker which catalyzed olefin epoxidation and a Zn-porphyrin pyridyl linker responsible for CO_2 insertion into the epoxide [91]. As opposed to traditional solvothermal syntheses, the authors obtained the MOF as a thin film using a layer-by-layer (LbL) growth approach, which resulted in a greater degree of variation in particle size and orientation that impacted the kinetics of the tandem process. Utilizing *p*-methoxystyrene as a substrate, the cycloaddition product 4-(4-methoxypenhyl)-1,3-di oxolan-2-one formed in > 60% yield. Without CO_2, overoxidation of the substrate occurred. However, under optimal conditions (60 atm CO_2, 65 °C, 14 h, 0.1 mol% ZnMn-porphyrin-based MOF, Table 1 entry 12), only trace side products formed, suggesting the Mn- and Zn-porphyrins act together to achieve product selectivity.

Over the past decade, metalloporphyrin MOFs have demonstrated their efficacy in biomimetic reactions inspired by the P450 oxidation pathway, in many cases sustaining high activity under mild conditions over multiple reaction cycles. Owing to the solid-phase nature of the highlighted MOFs, their use as heterogeneous catalysts also allows for ease of separation from a reaction mixture, simplifying purification procedures and enabling catalytic recyclability. Furthermore, their porous nature affords substrate access to a high density of metalloporphyrin centers, enabling catalytic competency at low catalyst loadings. However, to-date, some limitations still include the difficulty in directly activating molecular oxygen, a task accomplished by various prosthetic groups and coenzymes in P450. Thus, co-catalysts or auxiliary oxidants are often required in conjunction with a MOF-based catalyst. Moreover, poor diffusion of larger substrates into the MOF pores containing the active sites lends to poor catalytic performance. However, MOF thin films (*vide supra*)[91,105] and "nanoMOFs" offer a promising route to overcome the limitation of poor diffusion [106–110].

4. Porphyrin-Based MOFs for Photocatalysis

Evolving as interesting building blocks for the structural design and subsequent application of metal–organic frameworks (MOFs), porphyrins offer versatile functionality that can be harnessed for visible-light responsive photocatalysis [39,111–123]. Owing in part to their conjugated macrocyclic structure, porphyrins possess several important features for catalysis, and in particular for photocatalysis, including: (i) exposed metal sites, (ii) strong

visible-light absorption, (iii) long-lived excited states, (iv) high triplet quantum yield, and (v) the ability to act as redox-active photosensitizers [118,124]. The potential applications of porphyrin- and metalloporphyrin-containing MOFs in heterogeneous photocatalysis include hydrogen evolution [43,125], carbon dioxide reduction [126,127], oxidation *via* singlet oxygen production [65,128–132], alcohol oxidation [133], and Fenton-type chemistry [134,135] amongst others. Although this section focuses on experimental examples of photocatalytic porphyrin-based MOFs, it should be noted that the use of computational chemistry has been important to allow for the elucidation of photocatalytic mechanisms and to screen parameters for increasing the efficiency of photocatalytic activity [136,137]. An early example highlighting the ability of porphyrinic MOFs to harvest light across the entire visible spectrum was demonstrated by Lee *et al.,* where a pillared-paddlewheel type Zn-based MOF comprised of boron-dipyrromethene (BODIPY) and porphyrin-based struts was synthesized [40]. Around the same time, the first study demonstrating the photocatalytic properties of metalloporphyrin-based MOFs was published, focusing on the photo-oxidation of phenols and sulfides *via* the production of singlet oxygen [138]. In this example, Sn(IV)-porphyrin linkers were incorporated in a Zn-based MOF giving rise to a 3D framework capable of producing singlet oxygen under Xe lamp irradiation, and subsequently oxidizing 1,5-dihydroxynaphthalene and various aryl sulfide substrates. Building on these early examples of light harvesting and photocatalysis, herein, various examples of photocatalytic MOFs comprised of porphyrinic building blocks will be discussed.

4.1.   Photocatalytic hydrogen evolution

With the goal of moving towards the use of renewable energy sources to alleviate climate change, porphyrin-based MOFs bring about a promising opportunity for the photocatalytic generation of H_2 from water [139–144]. In 2012, Fateeva *et al.* constructed a water-stable porphyrinic MOF, Al-PMOF, comprised of tetrakis(4-carboxyphenyl)-porphyrin (H_4TCPP) linkers and Al(OH)O_4 chain nodes (Fig. 8) [43]. The free-base and Zn-porphyrin derivatives of Al-PMOF were both studied for the photocatalytic evolution of H_2 from water. In order to utilize the energy of the porphyrin-based excited states, a MOF/EDTA/Pt system was employed, where ethylenediaminetetraacetic acid (EDTA) was used as a sacrificial electron donor to reductively quench the excited state of the porphyrin molecules. The excited electron from the porphyrin could then be transferred to Pt, which was found to evolve H_2 from water at a rate of 100 µmol $g^{-1}h^{-1}$ (Zn-porphyrin) or 200 µmol $g^{-1}h^{-1}$ (free-base porphyrin), after an induction period of about 3 h.

A unique method used to increase photocatalytic H_2 production in a porphyrin-based MOF was shown by Leng *et al.* in 2018, where an In-based MOF comprised of In-oxo chain nodes and H_4TCPP linkers, USTC-8(In), was synthesized [125]. The porphyrinic linkers of USTC-8(In) were metallated with an out-of-plane (OOP) In^{3+}, different from conventional metallated porphyrins where the metal is in the plane of the porphyrin ring. The OOP In^{3+} was shown to be advantageous for the photocatalytic production of H_2 from water under visible-light irradiation, as USTC-8(In) demonstrated higher catalytic efficiency than the isostructural MOFs with in-plane metallation (USTC-8(M) M = Cu, Co, Ni) despite all the MOFs having the same LUMO level. The higher catalytic activity of USTC-8(In) was attributed to the OOP In^{3+} which was found to become detached from the porphyrin core

upon photoexcitation, thereby allowing for a longer charge separated state and avoiding the fast back electron transfer from the metal to porphyrin that is often detrimental to metalloporphyrinic MOF photocatalysts. The reduced In ions can then transfer electrons to a Pt co-catalyst which produces H_2 from water using triethylamine (TEA) as a sacrificial reductant to regenerate the free-base porphyrin. USTC-8(In) demonstrated a high photocatalytic activity for H_2 evolution of 341.3 µmol $g^{-1}h^{-1}$ in the presence of a Pt co-catalyst under visible-light irradiation – a rate up to 37 times higher than that of the in-plane metallated USTC-8 MOFs.

4.2. Photocatalytic carbon dioxide reduction

As a significant contributor to greenhouse gas emissions, carbon dioxide (CO_2) can instead be captured and photoreduced to give value-added products, a process that can be enhanced by the use of a MOF catalyst [124,145–160]. PCN-222 was not only able to capture CO_2 with moderate uptakes [126], it was also capable of catalytically reducing CO_2 to formate by using triethanolamine (TEOA) as a sacrificial reductant under visible-light irradiation (30 µmol of formate generated over 10 h) [126]. Ultrafast transient absorption (TA) spectroscopy and time-resolved photoluminescence (PL) spectroscopy studied the underlying mechanism of the photocatalytic reaction. Interestingly, electron trap states were observed in PCN-222, which can serve to enable electron-hole separation and store long-lived electrons for the photoreduction of CO_2. In a related system using MOF-525, metalation of the porphyrin with coordinatively unsaturated Co sites improved the efficiency of photocatalytic CO_2 reduction by increasing the amount of CO_2 adsorbed by the MOF [127].

4.3. Photocatalytic transformations using singlet oxygen

Singlet oxygen is an attractive reactive oxygen species that can be used for several catalytic transformations [161,162]. The ability to efficiently generate and increase the lifetime of singlet oxygen in catalytic systems is essential for its use in potential applications such as deprotection reactions [163], oxidation of sulfides [131,132,138] and phenols [128,138,164], as well as other organic contaminants [165]. In an early example demonstrating the production of singlet oxygen by a porphyrin-based MOF, Demel *et al.* reported a MOF, MOF-RE-TPPS, comprised of Eu_6-and Tb_6- clusters bridged by 5,10,15,20-tetrakis(4-sulfonatophenyl)por phyrin (TPPS) linkers (RE = rare-earth) [129]. It was found that the singlet oxygen produced by MOF-Eu-TPPS had a longer lifetime of 23 ± 1 µs, compared to that generated by TPPS intercalated in a Eu-based layered double hydroxide (LDH) structure (4 µs), confirming that coordination and rigid separation in a MOF may enhance the process of singlet oxygen generation. In addition, dehydration of MOF-Eu-TPPS decreased the singlet oxygen lifetime to 16 ± 1 µs, suggesting that singlet oxygen generation could be affected by MOF activation. In another example using RE-porphyrin-based MOFs for the production of singlet oxygen, 2D MOF nanosheets were synthesized using H_4TCPP and Ce^{3+}, Sm^{3+}, Eu^{3+}, Tb^{3+}, or Yb^{3+}, and it was found that thinner nanosheets led to better performance in the generation of singlet oxygen, an effect attributed to higher charge separation efficiency [128]. Owing to effective energy and electron transfer between the ligand and metal node, the < 13 nm thick Yb-based MOF nanosheet, Yb-TCPP-4, displayed the highest quantum yield of singlet oxygen production of 0.63. As a result, Yb-TCPP-4 was found to catalyze the oxidation of 1,5-dihydroxynaphthalene to juglone through the

production of singlet oxygen under visible-light irradiation (Xe lamp) with near complete conversion after 10 min.

In an example where the degree of porphyrin metalation was found to affect singlet oxygen production and subsequent catalytic activity, Johnson *et al.* demonstrated controllable metallation of an anionic In^{3+} porphyrin-based MOF, UNLPF-10, comprised of octatopic linkers (tetrakis-3,5-bis[(4-carboxy)phenyl]phenyl porphine (H_8TBCPPP)) and $[In(COO)_4]^-$ nodes (Fig. 9). UNLPF-10 is a unique structure built from Williams β-tetrakaidecahedral cages [65]. In order to evaluate the photocatalytic activity of the MOFs, the selective oxidation of aryl sulfides in open air (O_2) and under blue LED irradiation was studied. Of all the aryl sulfide substrates studied, thioanisole was the most promising, with complete and selective conversion to the sulfoxide occurring after 8 h of reaction using UNLPF-10–98 as a catalyst (porphyrin 98% metalated with In (III)). In contrast, when UNLPF-10–25 and UNLPF-10–71 were used as catalysts, the complete conversion of thioanisole required ~ 40 and 24 h of reaction, respectively. In a follow-up study, Johnson *et al.* looked at the effects of metalation of UNLPF-10 on the electronic structure and photoexcited states of the porphyrin-based MOF [130]. It was demonstrated that it is possible to control the photoredox catalytic performance of these porphyrinic MOFs through the process of linker metalation with In(III) or Sn(IV), generating highly oxidative excited states that can be used in organic transformations such as of arylboronic acid hydroxylation, the Mannich reaction, and aerobic amine coupling.

Porphyrinic MOFs capable of generating singlet oxygen have also been used as heterogeneous catalysts for the photo-oxidation of alkyl sulfides, and more specifically the mustard-gas simulant, 2-chloroethyl ethyl sulfide (2-CEES) [131,132,166]. In one example, PCN-222 generated singlet oxygen in order to selectively oxidize 2-CEES into the relatively nontoxic product, 2-chloroethyl ethyl sulfoxide (2-CEESO) with a half-life of 21 min under air, and 13 min under O_2 using blue LED irradiation [131]. Building on this work, Buru *et al.* showed an improvement in the photo-oxidation of CEES using PCN-222 by increasing the intensity of the irradiation source, giving a half-life of 11 min for the selective conversion of 2-CEES to 2-CEESO under O_2, corresponding to initial turnover frequencies (TOFs) ranging from 8 to 14 $mol_{CEES}\ mol_{chromophore}^{-1}\ min^{-1}$ [132].

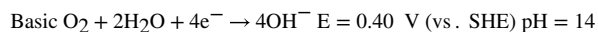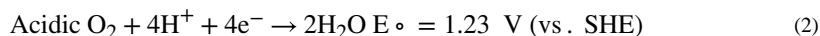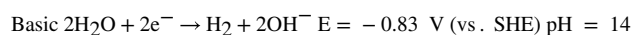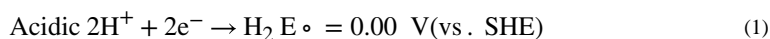## 5. Porphyrin-Based MOFs in Electrochemistry

The non-conductive nature of most MOFs challenges their potential applications within electrochemistry, yet reports of conductive MOFs nonetheless are promising for the emerging field [11]. To accomplish MOF-based electrochemical catalysis, researchers typically integrate the catalysts, such as porphyrin-containing MOFs, onto a conductive substrate for electrochemical catalysis. This can be accomplished through forming a composite material incorporating conductive Nafion, graphene oxide, or carbon nanotubes with previously synthesized MOFs, or through the direct growth of MOFs on conductive electrode substrates. Researchers must delicately balance the amount of conducting material with the added MOF electrocatalyst to ensure the entire MOF behaves as an efficient electrocatalyst. When this occurs, the electroactive surface area present in MOF systems

($\sim 10^{-8}$-10^{-7} mol/cm^2) is orders of magnitude higher than porphyrin single-molecule catalysts (10^{-11} mol/cm^2) [167].

5.1. Electrocatalytic hydrogen and oxygen evolution

Significant attention has shifted toward the use of hydrogen gas (H$_2$) as a clean source of energy for a fuel source, yet it is currently produced *via* steam reforming at high temperature (1000 °C) and pressures (20 bar). Alternatively, electrocatalysis requires less-demanding conditions to produce hydrogen gas with the potential for implementation in homes, vehicles, and remote locations.

Production of hydrogen gas from environmentally benign and abundant water occurs *via* the hydrogen evolution reaction (HER) in which protons (H$^+$) are reduced to hydrogen gas [168]. Equation 1 demonstrates the potential of the HER half reaction in acidic and alkali media. Catalytic systems based on precious metals (*e.g.*, Pt, Re, Ru, and Ir [169,170]) significantly reduce the overpotential (η), but the high cost and scarcity of these materials hampers the realization of low cost energy production systems. In aqueous media, the ideal oxidation reaction at the counter electrode for HER is the oxygen evolution reaction (OER; Equation 2 - reverse) [171]. However, OER often suffers from slow kinetics that require various electron transfer steps with high overpotential [172], creating a bottleneck in HER. Additionally, pH plays a significant role in these reactions; the abundance or lack of protons can significantly change the reduction potentials (Equation 3). As with HER, scarce and high cost materials such as IrO$_2$ and RuO$_2$ serve as the most efficient electrocatalysts for OER [172,173]. Thus, improved and practical HER and OER processes require alternative and highly stable catalyst systems based on more abundant metals.

$$\text{Acidic } 2H^+ + 2e^- \rightarrow H_2 \text{ } E\degree = 0.00 \text{ V(vs. SHE)} \tag{1}$$

$$\text{Basic } 2H_2O + 2e^- \rightarrow H_2 + 2OH^- \text{ } E = -0.83 \text{ V (vs. SHE) pH} = 14$$

$$\text{Acidic } O_2 + 4H^+ + 4e^- \rightarrow 2H_2O \text{ } E\degree = 1.23 \text{ V (vs. SHE)} \tag{2}$$

$$\text{Basic } O_2 + 2H_2O + 4e^- \rightarrow 4OH^- \text{ } E = 0.40 \text{ V (vs. SHE) pH} = 14$$

$$E = E\degree - 0.059 \text{ V} \times \text{pH} \tag{3}$$

Molecular species based on earth abundant metals such as Fe, Co, Ni, Mo and Mn [173–175] have catalyzed both HER and OER. Incorporating these molecular catalysts into MOF frameworks ensures that an electrode offers a high density of well-defined catalyst sites with optimal mass-transport for incoming (protons, or water /hydroxide) and outgoing (hydrogen, or oxygen) reagents in HER/OER. Furthermore, porphyrin-containing MOFs, have been

utilized in HER and OER applications due to their stability and the open face of the metal active site.

Given the efficacy of cobalt-metalated porphyrins for HER [176,177], Lin and co-workers [59] synthesized $Hf_{12}O_8(\mu_3\text{-OH})_8(\mu_2\text{-OH})_6(CoDBP)_9$, a MOF formed between a Hf^{4+} cluster-containing node and a Co^{3+}-metalated porphyrin. The MOF formed on carboxylic acid-terminated multi-walled carbon nano tubes (MWCNTs) before its deposition onto a glassy carbon electrode; Nafion was also incorporated to increase long-term stability. When investigating the reactivity of the Co sites for HER, the composite illustrated a 100-fold increase in the number of active sites as compared to an electrode made with the pristine MOF. The study suggested conductivity within the MOF proceeds through a charge hopping mechanism. Upon reduction of the Co^{2+} to Co^+, HER occurred through the protonation of the Co^+-H intermediate, and the composite material exhibited a high activity for HER (0.1 M perchloric acid, pH = 1). This electrocatalyst displayed an overpotential of 0.65 V at a current density of 10 mA/cm^2, stable hydrogen production, and negligible change in the current density for 7 h. At an overpotential of 0.715 V, a turnover number (TON) of 32,000 in 30 min and a turnover frequency (TOF) of 17.7 s^{-1} was observed with nearly no leaching of Hf and Co after 1 h, rendering this MOF as a competitive electrocatalyst.

The high density of catalytic sites in MOFs position the scaffolds as a way to overcome the poor kinetics associated with OER. Morris and co-workers grew a 30 μm film of PCN-224(Ni) on fluorine-doped tin oxide (FTO) [178]. The MOF particles become mechanically attached to the surface of the electrode during the synthesis process, enhanced by the pre-formation of a Ni-TCPP monolayer on the FTO surface. PCN-224(Ni) films displayed an onset overpotential of 0.450 V for OER. The reaction demonstrated pH independence in pH 3–10, suggesting electron transfer as the likely rate determining step in the reaction or dependent on the adsorption/-substitution chemistry on the active site. The MOF exhibited an exchange current density of 7.7×10^{-7} mA/cm^2, comparable to other heterogenous OER catalysts [179]. The observed low TON for the reaction (0.72) suggested water oxidation relies on the cooperative behavior of the Ni-TCPP active site and available proton binding sites on the Zr_6 oxo cluster, consistent with similar processes observed in other applications [180,181]; alternatively, the Zr-cluster could serve as a proton transfer medium.

Controlled potential electrolysis at 1.5 V (vs. SHE) for 1 h illustrated little change in the current density. X-ray photoelectron spectroscopy (XPS), scanning electron microscopy (SEM), and inductively coupled plasma mass spectrometry (ICP-MS) of the PCN-224(Ni) thin film catalyst post-electrolysis demonstrated a retention in the redox state and coordination geometry, morphology, and composition. However, ICP analysis indicated a gradual exfoliation of the MOF layer from the FTO.

Another example revisited the efficacy of a Co-porphyin derived MOF catalyst; Dehghanpour examined PCN-224(Co) for OER [182]. The electrocatalytic activity of PCN-224(Co) on a glassy carbon electrode was measured in a borate buffer solution at pH = 9.2. To achieve a current density of 2 mA/cm^2, a voltage of 1.55 V (vs. SHE) was necessary. The addition of MWCNTs to form a composite material greatly reduced the potential needed

to achieve 2 mA/cm^2 by 340 mV (Table 2). The authors observed a>3-fold increase in current density for the composite at 1.70 V (vs. SHE). The MOF/MWCNT composite material demonstrated a considerable increase in OER owing to the increase in electrochemical active surface sites.

Below pH 11, the PCN-224(Co)/MWCNT composite was exposed to a constant potential of 1.20 V (vs. SHE; $\eta = 0.500$ V) for 1 h, and the MOF showed little change in the current density. The electrode material lacked evidence indicating the formation of cobalt oxide or any leaching of cobalt into solution, highlighting the strong adhesion of the composite electrode to the GCE ideal for real-world applications.

5.2. Electrocatalytic oxygen reduction reaction

The oxygen reduction reaction (ORR) remains a key process in understanding and mimicking biological mechanisms [185], as well as the key cathodic reaction in various fuel cells. With few catalysts able to match its performance, Pt is largely considered the benchmark ORR electrocatalyst [186]. To address the technical and financial drawbacks of Pt-based electrocatalysts, research toward implementing transition-metal catalysts, particularly metal porphyrins, within ORR has made considerable progress [187]. As such, installing these molecular catalysts into a MOF should create a high density of active reaction sites able to further overcome the sluggish kinetics.

PCN-222(Fe) grafted onto 4-styrylpyridine-modified graphene (G-dye), exhibiting good activity for the 4-electron (Equation 2), single-step ORR pathway under alkali conditions [188]. With a 50 wt% mixture of MOF and graphene, the catalyst exhibited the earliest ORR onset (0.157 V vs. SHE) and the highest current density (–6.2 mA/cm^2 at –0.765 V vs. SHE) relative to other composites, the bare MOF, the modified graphene, and a MOF unmodified graphene composite (Table 3). This work highlights the importance of a good interface between MOF and substrate as well as the need to optimize the catalyst: graphene ratio to enhance the number of active MOF catalysts. Under acidic conditions, PCN-222(Fe) with a similar carbon composite [189] (pyridine-modified graphene, G-py) exhibited an onset potential of 0.495 V vs. SHE and a current density of –3.55 mA/cm^2 at 0.317 V vs. SHE. Impressively, PCN-222 (Fe) exhibited no change in electrochemical response when exposed to 3 M MeOH in both acidic and alkaline conditions, whereas Pt/C suffered from this catalyst poisoning. Thus, the MOF served as a more stable and chemically resistant electrocatalyst than traditional Pt catalysts.

Recognizing that graphene may limit the electrochemical accessibility of the active sites within the MOF, a previously studied OER MOF catalyst, PCN-224(Co)/MWCNT (Fig. 10), was tested for ORR activity [182]. With enhanced electron transfer kinetics, electrode stability, and good solution dispersion for electrode modification, the composite achieved an adequate ORR onset potential of 0.375 V vs. SHE and a roughly 6.4-fold current enhancement of a bare glassy carbon electrode. To demonstrate the importance of using a MOF, the authors explored CoTCPP/MWCNT composites. These composites delaminated from the electrode surface, whereas PCN-224(Co)/MWCNT remained attached to the electrode surface and exhibited good stability after 1 h of electrolysis.

Further work by Morris and team examined PCN-223 with the freebase and the iron-metalated porphyrin [190]. Under argon, the iron-containing MOF exhibited a redox peak for the Fe^{2+}/Fe^{3+} redox couple. Upon the introduction of oxygen to the solution, the Fe^{2+}/Fe^{3+} redox couple disappeared with a concomitant increase in current density due to ORR ($E_{onset} = -0.4$ V vs. SHE; Table 3); this phenomenon suggested the electrogenerated Fe^{2+} rapidly reacts with dissolved oxygen. The authors further explored the role of acid (trichloroacetic and acetic acid) as proton sources in ORR. In the presence of acid and O_2, the current density increased 100-fold with the catalytic onset occurring immediately after the Fe^{3+} reduction (–0.32 V vs. SHE for acetic acid, and –0.49 V for trichloroacetic acid). Furthermore, although trichloroacetic acid facilitated higher currents, it demonstrated poor selectivity for water in this reaction and (34% H_2O_2 with trichloroacetic acid compared to only 6% with acetic acid).

5.3. Electrocatalytic carbon dioxide reduction

With atmospheric carbon dioxide concentration increasing annually and the ever-growing global need for energy and fuel, platforms which address both concerns remain of high interest. For example, the electrochemical reduction of carbon dioxide (CO_2RR) to valuable feedstocks, fuel precursors, or directly into fuels accomplishes both aims. Metalloporphyrins have been extensively studied for CO_2RR [192], motivating their incorporation into MOFs to create next-generation CO_2RR catalysts. The wide range of products afforded from different amounts H^+ and e^- requires highly efficient and selective CO_2RR processes [193]. CO_2 transformations relevant to this review are shown in Equations 4–6. Much like HER and ORR, the potential of the reaction, E, is affected by pH in aqueous electrolytes and pK_a of the strongest acid in non-aqueous conditions [194].

$$CO_2 + 2H^+ + 2e^- \rightarrow CO + H_2O \quad E° = -0.106 \text{ V (SHE, aq.)} \tag{4}$$

$$CO_2 + 2H^+ + 2e^- \rightarrow CO + H_2O \quad E° = -0.65 \text{ V (SHE, MeCN)} \tag{5}$$

$$CO_2 + 2H^+ + 2e^- \rightarrow HCOOH \quad E° = -0.25 \text{ V (SHE)} \tag{6}$$
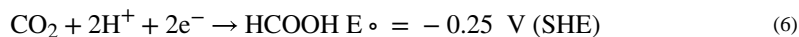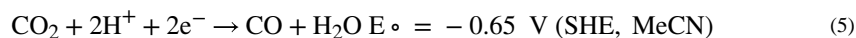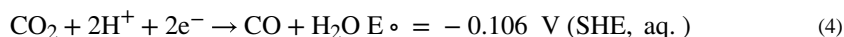
PCN-222(Fe) was incorporated with Vulcan XC72 (carbon black) and Nafion to form a composite material for CO_2RR [195]. This strategy achieved a faradaic efficiency for carbon monoxide of 91% at a current density of 1.2 mA/cm^2 (Table 4). A mere decrease in efficiency to 80.4% only after 10 h at –1.04 V vs. SHE (overpotential = 0.5 V) with a TOF of 50 CO molecules per hour demonstrated the long-term stability of the material as well as the particularly facile nature of constructing this electrode system. Further tailoring MOF design can likely yield additional high-performing systems with this strategy.

Beyond the production of carbon monoxide, the conversion of CO_2 can yield other value-added products of interest. Featuring a copper-containing MOF (node and porphyrin core), nanosheets of $Cu_2(CuTCPP)$ were grown on FTO for the electroconversion of carbon dioxide to formate and acetate (Fig. 11) [196]. Utilizing both Cu-paddlewheel-type nodes

and Cu-porphyrin linkers promoted synergistic electrocatalysis. At −1.0 V vs. SHE (4.5 mA/cm^2), the MOF nanosheets achieved TOFs of 2037 and 148 h^{-1}, with a Faradaic efficiency of 68.4 and 16.8% for formate and acetate respectively (Table 4). A look at the copper species in the MOF indicated the nanosheets underwent reconstruction to introduce CuO, Cu_2O, and Cu_4O_3 units within the material with no leaching of TCPP into solution. Although the MOF structure evolved during catalysis, it achieved a more effective overall catalyst.

Grown on FTO with no additional conductive material, MOF-525(Fe) (Table 4) was thoroughly studied for CO_2RR to carbon monoxide [167]. A current density of 5.9 mA/cm^2 at E = −1.3 V vs. SHE (0.65 V overpotential) with a TOF of 475 CO molecules per hour was observed in the presence of a proton source. The total Faradaic efficiency of this system was reported to be ~ 100% (40% CO and 60% H_2 production). This ratio of gases presents an interesting avenue for tandem catalysis to produce hydrocarbons *via* the Fischer-Tropsch reaction. MOF-525(Fe) exhibited charge diffusion in the MOF with Fe^0 as the catalytically active form. The first reduction from Fe^{3+} to Fe^{2+} occurred 20 times faster than the Fe^{1+} to Fe^0 reduction. Thus, future work should seek to improve charge and proton diffusion through MOFs to attain high turnovers with these highly efficient systems.

5.4. Other electrocatalysis

The use of porphyrin MOFs in other electrochemical applications accomplished the electrocatalytic detection of hydrogen peroxide, uric acid, xanthine, and hypoxanthine or even the reduction of other inert moieties [198]. Additionally, Morris and co-workers grew a Co-TCPP-based MOF on a conductive substrate. The MOF displayed an impressive conductivity consistent with a wide bandgap semiconductor. A detailed look at the electrochemistry resulted in an apparent diffusion coefficient of 7.55 ×10^{-14} cm^2/s, which is reasonable for a redox hopping mechanism. As a proof of concept, the MOF reduced carbon tetrachloride.

6. Porphyrin MOFs for Sensing Applications

The multifunctionality of porphyrins and the high porosity of MOFs position porphyrin-based MOFs as ideal candidates for sensing-related applications. Specifically, the unique catalytic, electrochemical and photophysical properties accessible in porphyrin scaffolds result in diverse sensing mechanisms (Fig. 12) [9,199]. As a result, installation of active porphyrin sites inside MOFs offer numerous advantages. For example, the multidimensional nature of MOFs can isolate the porphyrins and eliminates their aggregation, compared to solution-phase porphyrins, hence improving the reliability and accuracy of the MOF-based sensing. Owing to the high porosity inherent to MOFs, rapid analyte diffusion into the pores enhances their interaction with the porphyrin recognition sites and reduces the response time while increasing sensitivity. Moreover, the high tunability of MOFs enables facile modifications with other desired functional groups. With growing interest in constructing such frameworks, a large library of highly stable porphyrin MOFs exist to date which serve as high-performing sensing platforms for the detection of a variety of molecules and ions. In this section, we grouped the porphyrin MOF-based sensors into the following three

categories based on their functions: toxic chemical/pollutant sensing, pH sensing and biological sensing.

6.1.   Toxic chemical/pollutant sensing

Industrial discharge and agricultural runoff emit a variety of pollutants that pose health risks to human beings and animals. Among these pollutants, nitroaromatic explosives, pesticides, heavy metals, and anions can particularly exert toxic effects in humans even at low concentrations [200–202]. Therefore, developing methods to detect trace amounts of these compounds is essential for protecting the environment and human health. By employing the photophysical, catalytic and electrochemical properties of porphyrin MOFs, researchers demonstrated viable strategies for the detection and quantitative sensing of various toxic chemicals/pollutants.

Beyond serving as explosives in large quantities, nitroaromatic compounds pose as a highly toxic threat to living organisms requiring accurate and inexpensive detection [200]. To this end, porphyrin-based MOFs showed superior performance in sensing nitroaromatic explosives both in large quantities and at low concentrations [203,204]. A Zr(IV)-porphyrin MOF PCN-224 achieved the simple and rapid detection of 2,4,6-trinitrotoluene (TNT) in aqueous solution [203]. As a fluorescent sensor, PCN-224 quantitatively detected the concentration of TNT in water and offers high specificity even in the presence of other nitroaromatic explosives and ions. While TCPP provides strong interactions with TNT through hydrogen bonding and π-π stacking, the quantitative detection of TNT was based on the fluorescence quenching of PCN-224, a result of complexation between TNT and the porphyrin cores. In addition, the high surface areas of PCN-224 reduced the response time of the sensor (as short as 30 s) by facilitating the diffusion of TNT into the framework, thereby enhancing the analyte's interactions with TCPP. More recently, a series of lanthanide-based porphyrinic MOFs were also studied for the sensing of nitroaromatic compounds [204]. Particularly, a yttrium-based porphyrinic MOF exhibited efficient fluorescence quenching by nitroaromatic compounds and detected 2,4,6-trinitrophenol in trace amounts (0.82 ppm).

Traditional methods used for pesticides detection involve expensive equipment (*e.g.,* gas chromatography and high-performance liquid chromatography) and usually require a skilled workforce and complicated sample preparations, hindering rapid sensing on-site [205]. Porphyrin-MOFs act as fluorescence probes for the rapid and accurate detection of different pesticide families including organochlorines [206], organophosphates [207], and neonicotinoids [208]. Pentachlorophenol (PCP) is one representative organochlorine compound commonly used as an herbicide and insecticide. PCP undergoes slow degradation and poses as a highly toxic threat to humans, highlighting the need for an accurate detection of PCP in even trace amounts [209]. The first reported MOF-based sensor for PCP detection utilized PCN-222 (Zn), a MOF containing Zr_6 clusters as the metal nodes and Zn-TCPP as the organic linker, as a fluorescence probe [206]. This sensor rapidly detected (<30 s) trace amounts of PCP (as low as 33 ppb) in aqueous solution based on fluorescence quenching of PCN-222(Zn) by PCP. Similarly, a simple and rapid sensing platform for nitenpyram (a neonicotinoid pesticide) utilized the fluorescence quenching of nanoscale PCN-224 by the
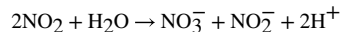
target analyte [208]. Again, this high-performing platform identified low concentration of nitenpyram in paddy water and soils with a detection limit of 0.03 μg·mL^{-1}.

Heavy metals persist as hazardous pollutants in wastewater, and they are highly toxic to humans even at low levels of exposure [201]. Taking advantage of the strong chelating effect between the porphyrin centers and metal ions, highly sensitive fluorescence probes incorporating porphyrin MOFs detected various heavy metals, including copper (Cu^{2+}) [210,211], mercury (Hg^{2+}) [212,213], chromium (in the form of $Cr_2O_7^{2-}$)[214] and cadmium (Cd^{2+}) [215,216]. In the detection of Cu^{2+}, for example, the porphyrins formed strong coordination bonds with Cu^{2+} which quenched the fluorescence of PCN-224 [210]. By measuring the fluorescence intensity of PCN-224 and comparing it to a reference signal emitted by another MOF UiO-66(OH)$_2$ encapsulated in PCN-224, the researchers determined the Cu^{2+} concentration in the sample with a detection limit of 0.068 nM. The strong affinity between porphyrins and Cu^{2+} resulted in this sensor's excellent chemical selectivity toward Cu^{2+} and implementation in a more complex environmental analysis. Beyond targeting Cu^{2+} as an analyte, similar strategies in utilizing fluorescence quenching-based MOF probes in other porphyrin frameworks were demonstrated for the detection of Hg^{2+}, $Cr_2O_7^{2-}$ and Cd^{2+} in water [212–216].

Beyond the aforementioned target cationic analytes, researchers designed fluorescence and electrochemical MOF sensors for the detection of anionic pollutants such as phosphate [217], nitrite [218] and bromate [216]. In these sensing processes, the multifunctional porphyrin MOFs acted as fluorophores [217], electrochemical catalysts [218], or molecular hosts [216]. One such representative sensor for phosphate detection utilized nanoscale PCN-222 nanorods (~80 nm × 240 nm, diameter × length) containing Zr_6 nodes and porphyrin linker TCPP [217]. Due to the strong affinity between phosphates and Zr_6 nodes, Zr-phosphate bonds replaced Zr-carboxy bonds from the TCPP linker in PCN-222 upon exposure to phosphate. Thus, the MOF decomposition released free TCPP linkers into the solution and emitted enhanced fluorescence allowing for the quantification of phosphate concentrations. This sensor exhibited good sensitivity for phosphate with a detection limit of 23 nM. Due to the biocompatibility and low cytotoxicity of PCN-222, the researchers also utilized the framework for the intracellular imaging of phosphate.

Electrochemical-based detection methods have also been exploited in porphyrin-contained MOFs. One such example is nitrite detection. Nitrite is one of the preservatives and additives used in food products. However, due to the harmful health effects of nitrites, monitoring these compounds are important [219]. Ho and co-workers grew a MOF-525 thin film for nitrite detection in 0.1 M KCl; [218,220] the porphyrin linker in the MOF acts as the active site for the oxidation of nitrite to nitrate with the following proposed mechanism.

$$2TCPP \rightleftharpoons 2TCPP^+ + 2e^-$$

$$2TCPP^+ + 2NO_2^- \rightarrow 2NO_2 + 2TCPP$$

$$2NO_2 + H_2O \rightarrow NO_3^- + NO_2^- + 2H^+$$
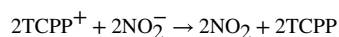
In the first step, the free base TCPP oxidizes into the cation. In the presence of the nitrite anion, the peak current at 1.05 V (SHE) increases linearly with the concentration of the nitrite. With the nitrite present in the electrolyte, diffusion of the nitrite ions into the MOF thin film occurs faster than charge hopping between the TCPP linkers; the subsequent oxidation of nitrite regenerates the TCPP from the TCPP$^+$. The sensing application of MOF-525 (Table 5) to the nitrite anion results in the linear relationship between concentration and current density from 20 to 800 μM with sensitivity of 95 μA/mMcm^2 and detection limit (LOD) of 2.1 μM (S/N = 3).

To reduce the low charge transfer rate between the linkers in MOF-525, researchers utilized a nanocomposite consisting of MOF-525 nanocrystals interconnected by<10 nm wide graphene nano ribbons (GNRs) [221]. Compared with the pristine MOF-525 thin films, the composite MOF-525/GNR electrodes (Table 5) generated higher current density at the lower onset potentials in the presence of nitrite. This sensor demonstrated a linear range of 100–2500 μM, sensitivity of 93.8 μA/mMcm^2, and LOD of 0.75 μM (S/N = 3). Compared with their previous study as well as most of the other nitrite sensors in aqueous media and neutral pH reports, this sensor exhibited a wider linear range.

Beyond Zr-based MOF-525, a Zn-based MOF (node and metalated porphyrin) was also explored for nitrite detection [222]. At an applied potential of 1.04 V (vs. SHE), the MOF (Table 5) displayed a sensitivity, detection limit, and the linear range of 158.1 μA/mM·cm^2, 0.26 μM (S/N = 3), and 1 μM–2 mM respectively. Of note, the 0.26 μM detection limit is among the lowest reported catalysts for nitrite detection. Moreover, catalytic oxidation of competing NO_3^-, SO_4^{2-}, SO_3^{2-}, $H_2PO_4^-$, Na^+, and K^+ species was not observed. The authors investigated the electrochemical sensor with real water samples (tap water, bottled water, and lake water), with a recovery of 93–109%.

6.2. pH sensing

Medical diagnostics and environmental analysis require accurate and reliable pH sensing. Porphyrin MOFs with superior chemical stability over a broad pH range emerge as viable candidates for pH sensing. Typically, these MOFs contain high-valence metal cations (*e.g.*, Zr^{4+}, Fe^{3+}, and Al^{3+}) and porphyrin-containing carboxylate linkers [42], and their pH sensing function primarily relies on the unique properties of porphyrins. Specifically, the protonation/deprotonation of the inner nitrogen atoms in a freebase porphyrin impacts the shape and electronic structure of the π-conjugated system. Such changes in their photophysical properties can be quantified by spectroscopic or colorimetric measurements of the MOFs [51,223].

To date, several Zr^{4+}-porphyrin MOFs have been studied as pH sensors, and the robust Zr(IV)-oxyanion bonds in these MOFs allow their structures to remain intact over a wide pH range [51,223,224]. With stability in the pH range of 1–11, one such Zr-porphyrin MOF, PCN-225, showed pH sensing capability with the most accurate range between pH 7 and 10

[51]. The protonation-deprotonation equilibrium of the porphyrin resulting from the different pH environment gave rise to a change in fluorescence of PCN-225 to quantify the pH sensing. Another Zr-porphyrin MOF PCN-222 exhibited colorimetric and luminescent responses when exposed to different pH conditions, serving as a reliable and reversible solid-state sensor for pH detection of pH 0 to 6 [223]. A third Zr-porphyrin MOF PCN-224 functionalized with an additional fluorescent ligand (rhodamine B isothiocyanate) demonstrated highly sensitive dual emission fluorescence within pH 1–11. This functionalized MOF also possessed low toxicity and ideal pH sensitivity when tested intracellularly in HeLa cells [224].

6.3. Biological sensing

For clinical diagnosis, early intervention of diseases and evaluation of therapeutics is of great interest to develop accurate and reliable sensing devices for relevant biological substrates. In the past few years, novel platforms based on porphyrin-MOFs have been reported for the quantitative detection of diverse biomolecules [225–235], antigens [236,237], enzymatic activity [238–241] and for intracellular chemical sensing [242–245]. In general, these methods rely on the accurate and selective recognition of the target substrate, as well as a sensitive and quantifiable response to the analyte molecules. By capitalizing on the unique electronic, photophysical and catalytic properties of the porphyrin MOF, fluorescence or electrochemical responses from the MOF can determine the substrate concentrations. In addition, the high tunability of porphyrin MOFs enables easy functionalization, allowing for further optimization of the sensors for selectivity and sensitivity.

Porphyrin MOFs offer a viable platform for sensing various biomolecules such as diagnostic biomarkers [226–230,236,237] and cancer cells [246]. To achieve specific recognition for a desired biomolecule, researchers modify the MOF with an appropriate aptamer. For example, in the detection of heparin (an anticoagulant), a 2D nanosheet MOF (Zn-TCPP(Fe)) physically adsorbed a heparin-specific AG73 peptide, which inhibited the peroxidase activity of the MOF by blocking its iron porphyrin active sites (Fig. 13) [227]. Upon exposure to heparin, AG73 peptides formed strong interactions with the heparin and dissociated from the MOF, thus exposing the MOF active site. In the presence of hydrogen peroxide, Zn-TCPP(Fe) then catalyzed the oxidation of Ampliflu Red to Resorufin, fluorescing at 585 nm. The fluorescence signature of Resorufin quantified the concentration of heparin, and the researchers further utilized this accurate and highly selective diagnostic platform to monitor the heparin activities in live rats. Similarly, Ou *et al.* utilized PCN-224 as a catalyst which also contained DNA linked dual aptamers serving as the recognition site for the detection of MCF-7 cells [246]. Their strategy demonstrated a low detection limit for breast cancer cells (6 cells/mL) potentially utile for early cancer diagnosis. Furthermore, the electrochemical properties of porphyrin MOFs and a carbon electrode functionalized with recognition sites facilitated the electrochemical sensing of DNA [229] and microRNA [226].

The approach of coupling porphyrin MOFs with functionalized electrodes further accomplished the sensing of antigens, giving rise to enzyme-free immunosensors with high sensitivity. One such photoelectrochemical immunosensor was created by Zhang *et al.* for

the detection of prostate specific antigen (PSA), a diagnostic biomarker for prostate cancer [236]. In this study, a DNA-tagged anti-PSA antibody coordinated to the Zr_6 nodes of a nanoscale Zr-porphyrin MOF (PCN-222/MOF-545) served as a signaling probe for PSA. In the presence of PSA, the porphyrin MOF generated a cathodic photocurrent through a photoelectrochemical process proportional to the concentration of PSA. This highly sensitive and selective immunosensor detected PSA within the concentrations of 1 pg/mL to 10 ng/mL with a detection limit of 0.2 pg/mL. Using a similar approach, Chen *et al.* developed another highly sensitive photoelectrochemical immunosensor with nanosized PCN-224 for the detection of Human Epididymis Protein 4, a known biomarker of ovarian cancer [237]. In both studies, the research team discovered that the nanoscale of the porphyrin MOFs improved the performance of the sensors due to the enhanced interactions between the porphyrin units and the substrates.

Enzymes are biological macromolecules that catalyze a large variety of biochemical reactions [247]. Moreover, they largely regulate cellular processes and metabolism within organisms, and the malfunction in the expression of enzymes can lead to a multitude of diseases. Thus, monitoring enzyme activity levels is critical for the well-being of many individuals, requiring reliable sensing technologies. Toward this end, the incorporation of Zr MOFs containing metallated porphyrins linkers into highly sensitive biosensors has enabled the probing of kinase and telomerase activities [238–241]. Protein kinases catalyze protein phosphorylation, and abnormal activities of kinase was considered relevant to diseases such as cancers and Alzheimer's disease [248–250]. Therefore, the development of a sensitive and reliable probe for detecting kinase activities specifically is crucial for diagnosing related diseases and evaluating the therapeutic efficacy of kinase inhibitors. For this purpose, Zhang *et al.* designed an electrochemiluminescence (ECL) sensor that demonstrated excellent accuracy and reliability in biological samples (Fig. 14) [238]. The key component of the sensor, Zr-MOF-525(Zn) bearing Zn-TCPP linkers and Zr_6 metal nodes, served multiple functions in the sensing process. First, the highly porous MOF concentrated oxygen molecules into its cages, while the photoelectric active Zn-TCPP converted O_2 into $^1O_2$, giving rise to ECL signal. Meanwhile, the Zr_6 clusters of the MOF served as recognition sites for the phosphate groups in the samples resulting from the kinase-catalyzed phosphorylation reaction. It is worth noting that additional biological aptamers were not needed in this MOF sensor given that the Zr_6 clusters of the MOF recognized the substrate by forming strong coordinate bonds with phosphate. This bonding interaction led to enhanced ECL emission of the MOF, which quantified the kinase activity. Around the same time, the electrochemical activities of another MOF Zr-TCPP(Fe) also realized the simple and reliable sensing of telomerase activity [240,241], (Fig. 15).

Lastly, porphyrin MOFs have also been implemented in the intracellular detection of small molecules such as oxygen (O_2) [242], nitric oxides (NO) [243], hydrogen sulfide (H_2S) [245] and hydrogen peroxide (H_2O_2) [251]. These small molecules play unique and important roles in cellular metabolism. For example, O_2 maintains cellular life, and a lack of oxygen (hypoxia) is very detrimental to cellular life and can even lead to proliferation of cancer cells [252]. Nitric oxide and hydrogen sulfide serve as gaseous signaling molecules in multiple organ systems [253,254]. Hydrogen peroxide is a reactive oxygen species (ROS) that tends to concentrate in cancerous cells [255]. Developing methods that accurately

monitor the intracellular concentrations of these molecules will advance the understanding of their roles in cellular metabolism and the diagnosis of related diseases. For oxygen sensing, a nanoscale Hf MOF containing Pt(II)-metallated porphyrin linkers was functionalized with Rhodamine-B isothiocyanate (RITC) by conjugation with the quaterphenyldicarboxylate linker, yielding a modified mixed-linker MOF called R-UiO [242]. While the phosphorescent properties of the Pt-Porphyrins were dependent on the partial pressure of O_2, the oxygen independent fluorescence of the RITC ligand functioned as a reference. The nanoscale R-UiO showed good biocompatibility and achieved intracellular detection of O_2 with high accuracy. A very similar approach was used for the intracellular detection of nitric oxide [243].

Real-time detection of H_2S levels in living cells is crucial for understanding its function in physiological processes and its relation to neurological disorders such as Alzheimer's disease and Down's syndrome [256,257]. A stable nanoMOF containing Cu (II)-metallated porphyrin linkers and Al nodes served as a H_2S probe with high sensitivity and selectivity [245]. In the presence of H_2S, Cu(II)-porphyrins underwent protonation to produce CuS and freebase porphyrins. Thus, the fluorescence emitted by free-base porphyrins directly quantified the H_2S concentration because the Cu(II)-porphyrin does not fluoresce. This MOF sensor exhibited a strong linear relationship between 0 and 10 μM of H_2S with a detection limit of 16 nM at physiological pH (7.40). Further testing explored the sensor for intracellular H_2S detection in HepG2 and A549 cells using confocal imaging. The results illustrated the Al-porphyrin MOF serves as a biocompatible, selective and sensitive sensor for real-time detection of H_2S. By taking advantage of the Fe^{3+}-porphyrin's peroxidase activity, novel sensing platforms incorporating porphyrin-MOFs with Fe-metallated porphyrin linkers have been applied in the intracellular detection of H_2O_2 [244]. Particularly, the MOF served as a highly active electrocatalyst for H_2O_2 reduction, giving rise to a rapid amperometric response corresponding to H_2O_2 concentration. Later on, the peroxidase activity of porphyrin MOFs accomplished the quantitative sensing of glucose [231–233].

In summary, porphyrin MOFs and their derivatives have been instrumental in the detection of a wide variety of compounds and conditions, ranging from chemical pollutants to biological substrates and pH. In these sensing platforms, porphyrin MOFs or their components (*i.e.,* metal nodes and porphyrin linkers) served as a myriad of functions including a fluorescence/electrochemical probe, a catalyst, a recognition site, a host material, and/or a substrate material for desired functionalization. With ongoing advancements toward reducing the cost and fabrication complexity of these sensors as well as improving their reusability, porphyrin MOFs offer niche commercialization opportunities in environmental sensors, pH sensors, and medical diagnostic devices.

7. Porphyrin-Based MOFs in Biomedicine

Molecular porphyrins have enjoyed significant success in therapeutics (*i.e.,* the treatment of disease) [258]. As just one example, molecular porphyrins serve as exceptional photosensitizers for photodynamic therapy in clinical oncology [258,259]. However, poor stability *via* enzymatic degradation and/or molecular aggregation, poor cellular uptake, and

poor pharmacokinetics hinder molecular porphyrins, necessitating strategies to overcome these shortcomings [260].

MOFs containing porphyrin linkers have recently attracted attention as therapeutics in oncology as well as other areas [17,260–262]. Porphyrin linkers isolated within a solid MOF are less prone to enzymatic degradation, resist aggregation, and offer modifiable surface properties to impact cellular uptake. Furthermore, the porous nature of MOFs allows them to deliver therapeutic cargo. While still in its infancy, the field of porphyrin-containing MOFs as therapeutics and therapeutic delivery agents is rapidly evolving and has played a crucial role in the development of RiMO-301—a MOF currently in Phase I clinical trials for the treatment of advanced cancers [263,264]. Many important discoveries quickly pushed the field towards this exciting result, and we highlight some of the most important contributions that porphyrin-based MOFs offered to the field of MOF-based therapeutics, MOF-based therapeutic delivery, and synergistic MOF-based therapies.

7.1. Porphyrin-based MOFs as therapeutics

7.1.1. Photodynamic therapy—Photodynamic therapy (PDT) relies on delivering photosensitizers (PS) to target tissue cells, absorption of light to produce a photoexcited state, and subsequent generation of reactive oxygen species (ROS), such as singlet oxygen ($^1O_2$) as shown in Fig. 15. PDT functions therapeutically by inducing cell death, causing tumor infarction, and/or activating an immune response [258]. To date, a handful of researchers utilized MOFs containing porphyrin linkers for PDT and derived some important design principles [58,265–271].

Lu *et al.* first demonstrated that MOFs containing porphyrin linkers could be utilized for PDT [58]. The MOF, DBP-UiO (Fig. 16), was constructed with Hf_6-based nodes and the dicarboxylate linker, 5,15-di(p-benzoato)porphyrin (DBP). When irradiated with LED light (peak emission of 640 nm) DBP-UiO readily generated $^1O_2$. *In vitro* studies demonstrated the efficacy of DBP-UiO against head and neck cancer cells, while *in vivo* experiments showed complete tumor destruction in a xenograft murine mouse model. Lu et al.'s pioneering study identified several key PDT design principles that effectively increase cellular PS concentration and therefore $^1O_2$ generation. First, the heavy Hf_6-based nodes enhanced $^1O_2$ production by promoting intersystem crossing. Second, DBP-UiO exhibited a nanoplate morphology, ~100 nm in diameter and ~ 10 nm in thickness, which impacted $^1O_2$ generation by promoting diffusion of ROS. (Gains in $^1O_2$ generation are offset in larger MOF particles as ROS diffusion lengths increase [58]). Finally, locking porphyrin linkers within the MOF scaffolding prevents aggregation and subsequent deactivation via self-quenching.

Despite the exciting initial results from Lu et al., [58] porphyrin linkers do exhibit some significant photophysical challenges [260]. Most notably porphyrins often have low extinction coefficients (ε). Hydrogenation of the porphyrin core to produce so-called chlorins can drastically increase e. Therefore, Lu *et al.* subsequently hydrogenated DBP to produce 5,15-di(*p*-benzoato)-chlorin (H_2DBC) [265]. The resultant MOF, DBC-UiO, contained DBC linkers and Hf_6-based nodes. An 11-fold increase in ε was observed for DBC-UiO (chlorin linker) relative to DBP-UiO (porphyrin linker) which in turn lead to a 3-

fold increase in $^1O_2$ generation. While not rigorously a porphyrin linker, this work highlights rational MOF design strategies for improved PDT.

Park *et al.* demonstrated that MOF nanoparticle size directly influences cellular uptake [266]. Utilizing PCN-224, nanoparticles ranging in size from 30 nm to 190 nm were synthesized. Cellular uptake was carried out *in vitro* using human cervical cancer (HeLa) cells. Cellular uptake exhibited volcano plot behavior—the 90 nm PCN-224 particles exhibited the highest cellular uptake, while both larger and smaller particle sizes observed smaller cellular uptake. Upon irradiation with 420 nm light, the 90 nm sample also showed the highest PDT efficacy (81%).

7.1.2. Alternative strategies to generate ROS—While PDT successfully generates ROS, some challenges exist for its clinical use. For example, PDT is limited by poor tissue penetration depth which poses challenges in treating some tumors. Instead, radiation therapy (RT) uses X-rays, which offer better tissue penetration depth, to generate ROS and ultimately induce cell death. MOFs containing Hf_6-based nodes can absorb X-ray irradiation and transfer energy to its linkers [272]. Liu *et al.* took advantage of this principle by combining TCPP linkers and Hf_6-based nodes and subsequently modifying the MOF surface with polyethylene glycol (PEG) [273]. The resultant MOF (Hf-TCPP) generated ROS under RT and separately under visible light (*i.e.*, PDT). Combination RT/PDT therapy was effective *in vivo* against a breast cancer mouse model. Liu et al.'s study also demonstrated blood circulation lifetimes for Hf-TCPP of ~ 3 h and accumulation of Hf-TCPP in the liver and spleen. Fortunately, Hf was excreted from the liver and spleen. In a similar fashion, NIR light can also generate ROS [274].

Wang *et al.* demonstrated chemical generation of ROS from Cu-TCPP nanosheets, a 2-D MOF with Cu^{2+} nodes and Cu^{2+} metalated TCPP in the absence of light [275]. A stoichiometric reductant (glutathione, GSH) and oxidant (hydrogen peroxide) were both needed to generate ROS. Fortunately, cancer cells often contain reductants such as glutathione and oxidants such as hydrogen peroxide that can serve in this function. The authors proposed that $^1O_2$ was generated through the mechanism shown in Fig. 17. The precise source of Cu^{2+} (*i.e.,* from the nodes or linkers) was not identified; however Ni *et al.* demonstrated Cu^{2+} from the nodes in a similar MOF can produce ROS [276]. In the absence of applied visible light, Cu-TCPP was effective *in vivo* against a cervical cancer cell line.

7.2. Porphyrin-based MOFs for therapeutics delivery

Nanoscale MOFs containing porphyrin linkers have also become useful for the immobilization and storage of therapeutic agents [277–279]. For example, Wang *et al.* loaded insulin into the pores of the mesoporous MOF, PCN-222 [279], which they previously demonstrated prevents insulin degradation and can also release insulin under simulated physiological conditions [280]. A significant challenge in the therapeutic delivery of MOFs is their poor colloidal stability in combination with positively charged surfaces that often inhibit cellular uptake [279]. Wang *et al.* coated insulin loaded PCN-222 (*i.e.,* insulin@MOF in Fig. 4) with phosphate-terminated DNA strands to generate so-called insulin@DNA-MOF (also shown in Fig. 4). Phosphate-terminated DNA strands coordinate

to Lewis acidic Zr^{VI} ions (from the Zr_6-based nodes) located on the surface of the MOF [281,282]. Insulin@DNA-MOF was colloidally stable in a cellular medium for 24 h, while the unfunctionalized insulin@MOF aggregated in<1 h. In addition, the insulin@DNA-MOF exhibited superior cellular uptake in comparison to insulin.

Ning *et al.* utilized the same surface functionalization technique to decorate the surface of PCN-224 with DNA [278]. In this example, however, the therapeutic agent was simply attached to the exterior surface of the MOF. Again, phosphate-terminated DNA strands coordinated with Zr^{IV} ions on the surface of the MOF. DNA surface functionalization changed the surface potential of PCN-224 from positive (zeta potential 16.1 mV) to negative (zeta potential −27.8 mV). Subsequently, the DNA modified PCN-224 nanoparticles were hybridized with an anti-nucleolin DNA aptamer to produce so-called APT-NMOFs. The DNA aptamer enhanced cellular uptake in human breast cancer cells and directly functioned as therapeutic agent for DNA delivery.

7.3. Synergistic therapeutics using porphyrin-based MOFs

Not surprisingly, MOF-based therapeutics and MOF-based therapeutic delivery can work synergistically to provide improved outcomes [276,283–294]. Lu *et al.* demonstrated the possibility of PDT in combination with therapeutic delivery. TBC-Hf, a MOF constructed from 5,10,15,20-tetra(*p*-benzoato)chlorin linkers and Hf_6-based nodes, was used to encapsulate indoleamine 2,3-dioxygenase (IDOi) and produced IDOi@TBC-Hf. IDO is a small molecule inhibitor that induces checkpoint blockade immunotherapy (CBI)—an immunotherapy that relies on "therapeutic antibodies to disrupt negative immune regulatory checkpoints and unleash pre-existing anti-tumor immune responses" [295]. Lu *et al.* demonstrated the efficacy of TBF-Hf against a colorectal mouse model at treating localized tumors via PDT, while the release of IDOi inhibited both local and distant tumors via CBI (Fig. 18) [296]. This strategy was also successful when irradiating similar Hf-based MOFs with X-rays instead of visible light [287]. The Hf nodes absorb X-rays and produce ROS (*i.e.,* radiation therapy, RT) while concomitantly transferring energy to the porphyrin-based linkers to generate $^1O_2$ (*i.e.,* radio dynamic therapy, RDT). The combination RT/RDT/CBI therapy was highly effective against local and distant tumors in multiple mouse cancer models.

Synergistic therapy can also be achieved by loading a therapeutic agent on the exterior of the MOF. Li *et al.* synthesized a composite material termed mCGP composed of PCN-224 wrapped in glucose oxidase (GOx), catalase, and a cancer cell membrane [283]. The linkers in PCN-224 absorb light for PDT, however one of the challenges associated with PDT is the lack of oxygen in tumors that in-turn induces hypoxia (*i.e.,* insufficient oxygen supply). GOx and catalase on the surface of mCGP decompose hydrogen peroxide and glucose, often present in hypoxic cells, and ultimately produce $^1O_2$. The cancer cell membrane allows tumor specific targeting and changes the surface potential of PCN-224 from 24.5 mV to −20.9 mV. Under irradiation, mCGP was effective *in vivo* against a mouse breast cancer model. Several other studies reported the generation of $^1O_2$ under hypoxic conditions by MOFs containing porphyrin linkers [270,275,276,285,286,288,289,292].

Finally, synergistic therapy can be employed by coupling MOFs with intravenous immunotherapies [276,288,291,293]. For example, Zeng *et al.* synthesized TBP-MOF (TBP = tetrakis (4-carboxyphe nyl)tetrabenzoporphyrin) based on Zr_6-nodes and TBP linkers [288]. When wrapped in PEG, the nanosized MOF effectively generated $^1O_2$ under hypoxic conditions. When combined with αPD-1 CBI, TBP-MOF was effective against primary tumors while simultaneously suppressing metathesis in an *in vivo* mouse model. PDT and αPD-1 CBI triggered an immune response and actively recruited T-cells to suppress tumors. In addition, the authors challenged the immune effect by re-injecting metastatic cells back into the PDT/αPD-1 treated mice and observing the prevention of tumor recurrence.

8. Conclusions and Outlooks

The unique and versatile functionality of porphyrins, in combination with the high porosity and tunability of MOFs, position porphyrin-based MOFs as an ideal platform for the heterogenization of porphyrin species with precisely tailorable structures and properties. As a historical overview, the development of porphyrin-based MOFs in the past two decades or so, has evolved from structural explorations to their implementation in a wide variety of applications centered upon the biomimetic, photophysical, electrochemical, and bioactive characteristics of porphyrins. While these encouraging and exciting steps have been made in the field, challenges still remain for wider access to, and broader applications of, porphyrin-based MOFs.

Looking forward, some of the challenges in porphyrin-based MOFs align well with those in MOFs in general. Examples include lowering the production cost of porphyrin-based MOFs and enhancing their structural robustness, properties that are highly desirable for applications involving harsh conditions such as catalysis. To date, the high cost and low yield of porphyrin-based organic linkers, especially the ones with low-symmetry substituents, has hindered their applications on a broader scale. Wide access to porphyrin-based MOFs will undoubtedly facilitate the investigation of the photo-, electro-chemical and biological activities of porphyrins and metalloporphyrins, for their important roles in pollution remediation, solar energy conversion and biomedical therapeutics.

Studies on porphyrin-based MOFs have almost unanimously focused on the functionality of porphyrins thanks to their intrinsic advantages in the various applications discussed above. However, MOFs as porous platforms for the alignment and immobilization of porphyrin species are far from being exploited to their full potential. The nanosized space and unlimited additional properties brought about by the metal-based nodes as well as secondary functional organic linkers remains largely underexplored. For example, only a couple of studies have taken advantage of the multifaceted catalytic functionality of porphyrin-based MOFs for tandem catalysis [91,297].

Considerable research efforts on porphyrin-MOF catalysts has been inspired by the metalloporphyrin active sites of a variety of enzymes, yet the field can greatly benefit from targeting more complexed pore environments achievable in porphyrin-based MOFs. Specifically, MOF tunability offers opportunities to mimic not only the active sites of enzymes, but also the chemical environment that is close to the active center to achieve well-

defined mimicries of enzymes in their native states. To this end, porphyrin-based MOFs with controllable hydrophobicity, pendant amino acid groups and hierarchical pore structures offer unlimited opportunities to furnish the proximity effect toward the grand challenge of artificial enzymes.

Acknowledgements

References

[1]. Eddaoudi M, Kim J, Rosi N, Vodak D, Wachter J, O'Keeffe M, Yaghi OM, Science 295 (2002) 469–472. [PubMed: 11799235]

[2]. Chen Z, Li P, Anderson R, Wang X, Zhang X, Robison L, Redfern LR, Moribe S, Islamoglu T, Gómez-Gualdrón DA, Yildirim T, Stoddart JF, Farha OK, Science 368 (2020) 297–303. [PubMed: 32299950]

[3]. Lee J, Farha OK, Roberts J, Scheidt KA, Nguyen ST, Hupp JT, Chem. Soc. Rev 38 (2009) 1450–1459. [PubMed: 19384447]

[4]. Zhang X, Huang Z, Ferrandon M, Yang D, Robison L, Li P, Wang TC, Delferro M, Farha OK, Nat. Catal 1 (2018) 356–362.

[5]. Mon M, Bruno R, Ferrando-Soria J, Armentano D, Pardo E, J. Mater. Chem. A 6 (2018) 4912–4947.

[6]. Islamoglu T, Chen Z, Wasson MC, Buru CT, Kirlikovali KO, Afrin U, Mian MR, Farha OK, Chem. Rev 120 (2020) 8130–8160. [PubMed: 32207607]

[7]. Lian X, Fang Y, Joseph E, Wang Q, Li J, Banerjee S, Lollar C, Wang X, Zhou H-C, Chem. Soc. Rev 46 (2017) 3386–3401. [PubMed: 28451673]

[8]. Chen Y, Li P, Zhou J, Buru CT, Dordevic L, Li P, Zhang X, Cetin MM, Stoddart JF, Stupp SI, Wasielewski MR, Farha OK, J. Am. Chem. Soc 142 (2020) 1768–1773. [PubMed: 31927881]

[9]. Kreno LE, Leong K, Farha OK, Allendorf M, Van Duyne RP, Hupp JT, Chem. Rev 112 (2012) 1105–1125. [PubMed: 22070233]

[10]. Ko M, Mendecki L, Eagleton AM, Durbin CG, Stolz RM, Meng Z, Mirica KA, J. Am. Chem. Soc 142 (2020) 11717–11733. [PubMed: 32155057]

[11]. Sun L, Campbell MG, Dinc M, Angew. Chem., Int. Ed 55 (2016) 3566–3579.

[12]. Zhang X, Saber MR, Prosvirin AP, Reibenspies JH, Sun L, Ballesteros-Rivas M, Zhao H, Dunbar KR, Inorg. Chem. Front 2 (2015) 904–911.

[13]. Aulakh D, Pyser JB, Zhang X, Yakovenko AA, Dunbar KR, Wriedt M, J. Am. Chem. Soc 137 (2015) 9254–9257. [PubMed: 26167692]

[14]. Chen Z, Hanna SL, Redfern LR, Alezi D, Islamoglu T, Farha OK, Coord. Chem. Rev 386 (2019) 32–49.

[15]. Yaghi OM, A.C.S. Cent, Sci 5 (2019) 1295–1300.

[16]. Chen Z, Li P, Zhang X, Li P, Wasson MC, Islamoglu T, Stoddart JF, Farha OK, J. Am. Chem. Soc 141 (2019) 2900–2905. [PubMed: 30735359]

[17]. Zhu Y, Chen J, Kaskel S, Angew. Chem., Int. Ed (2020), 10.1002/anie.201909880.

[18]. Feng L, Wang K-Y, Joseph E, Zhou H-C, Trends Chem 2 (2020) 555–568.

[19]. Gao W-Y, Chrzanowski M, Ma S, Chem. Soc. Rev 43 (2014) 5841–5866. [PubMed: 24676096]

[20]. Norvaisa K, Kielmann M, Senge MO, Chembiochem 21 (2020) 1793–1807. [PubMed: 32187831]

[21]. Huang Q, Liu J, Feng L, Wang Q, Guan W, Dong L-Z, Zhang L, Yan L-K, Lan Y-Q, Zhou H-C, Natl. Sci. Rev 7 (2019) 53–63.

[22]. Huang H, Song W, Rieffel J, Lovell JF, Front. Phys 3 (2015), 10.3389/fphy.2015.00023.

[23]. Jasat A, Dolphin D, Chem. Rev 97 (1997) 2267–2340. [PubMed: 11848901]

[24]. The numbers of porphyrin-based MOFs are obtained from the MOF subset (including "1D, 2D, and 3D MOF and MOF-like structures with all kinds of pore sizes as well as nonporous structures") of CSD.

[25]. Li A, Bueno-Perez R, Wiggin S, Fairen-Jimenez D, CrystEngComm (2020), 10.1039/d0ce00299b.

[26]. Gropp C, Canossa S, Wuttke S, Gándara F, Li Q, Gagliardi L, Yaghi OM, ACS Cent. Sci 6 (2020) 1255–1273. [PubMed: 32875067]

[27]. Chen Z, Jiang H, Li M, O'Keeffe M, Eddaoudi M, Chem. Rev 120 (2020) 8039–8065. [PubMed: 32302477]

[28]. Abrahams BF, Hoskins BF, Michail DM, Robson R, Nature 369 (1994) 727–729.

[29]. Lin K-J, Angew. Chem., Int. Ed 38 (1999) 2730–2732.

[30]. Hagrman D, Hagrman PJ, Zubieta J, Angew. Chem., Int. Ed 38 (1999) 3165–3168.

[31]. Sharma CVK, Broker GA, Huddleston JG, Baldwin JW, Metzger RM, Rogers RD, J. Am. Chem. Soc 121 (1999) 1137–1144.

[32]. Goldberg I, CrystEngComm 4 (2002) 109–116.

[33]. Diskin-Posner Y, Dahal S, Goldberg I, Chem. Commun (2000) 585–586.

[34]. Goldberg I, Chem. Commun (2005) 1243–1254.

[35]. Kosal ME, Chou J-H, Wilson SR, Suslick KS, Nat. Mater 1 (2002) 118–121. [PubMed: 12618827]

[36]. Smithenry DW, Wilson SR, Suslick KS, Inorg. Chem 42 (2003) 7719–7721. [PubMed: 14632483]

[37]. Smithenry DW, Suslick KS, J. Porphyrins Phthalocyanines 08 (2004) 182–190.

[38]. Suslick KS, Bhyrappa P, Chou JH, Kosal ME, Nakagaki S, Smithenry DW, Wilson SR, Acc. Chem. Res 38 (2005) 283–291. [PubMed: 15835875]

[39]. Shultz AM, Farha OK, Hupp JT, Nguyen ST, J. Am. Chem. Soc 131 (2009) 4204–4205. [PubMed: 19271705]

[40]. Lee CY, Farha OK, Hong BJ, Sarjeant AA, Nguyen ST, Hupp JT, J. Am. Chem. Soc 133 (2011) 15858–15861. [PubMed: 21916479]

[41]. Farha OK, Shultz AM, Sarjeant AA, Nguyen ST, Hupp JT, J. Am. Chem. Soc 133 (2011) 5652–5655. [PubMed: 21446651]

[42]. Howarth AJ, Liu Y, Li P, Li Z, Wang TC, Hupp JT, Farha OK, Nat. Rev. Mater 1 (2016) 15018.

[43]. Fateeva A, Chater PA, Ireland CP, Tahir AA, Khimyak YZ, Wiper PV, Darwent JR, Rosseinsky MJ, Angew. Chem., Int. Ed 51 (2012) 7440–7444.

[44]. Cavka JH, Jakobsen S, Olsbye U, Guillou N, Lamberti C, Bordiga S, Lillerud KP, J. Am. Chem. Soc 130 (2008) 13850–13851. [PubMed: 18817383]

[45]. Bai Y, Dou Y, Xie L-H, Rutledge W, Li J-R, Zhou H-C, Chem. Soc. Rev 45 (2016) 2327–2367. [PubMed: 26886869]

[46]. Feng D, Gu Z-Y, Li J-R, Jiang H-L, Wei Z, Zhou H-C, Angew. Chem., Int. Ed 51 (2012) 10307–10310.

[47]. Morris W, Volosskiy B, Demir S, Gándara F, McGrier PL, Furukawa H, Cascio D, Stoddart JF, Yaghi OM, Inorg. Chem 51 (2012) 6443–6445. [PubMed: 22676251]

[48]. Feng D, Gu Z-Y, Chen Y-P, Park J, Wei Z, Sun Y, Bosch M, Yuan S, Zhou H-C, J. Am. Chem. Soc 136 (2014) 17714–17717. [PubMed: 25479454]

[49]. Deria P, Gómez-Gualdrón DA, Hod I, Snurr RQ, Hupp JT, Farha OK, J. Am. Chem. Soc 138 (2016) 14449–14457. [PubMed: 27768297]

[50]. Feng D, Chung W-C, Wei Z, Gu Z-Y, Jiang H-L, Chen Y-P, Darensbourg DJ, Zhou H-C, J. Am. Chem. Soc 135 (2013) 17105–17110. [PubMed: 24125517]

[51]. Jiang H-L, Feng D, Wang K, Gu Z-Y, Wei Z, Chen Y-P, Zhou H-C, J. Am. Chem. Soc 135 (2013) 13934–13938. [PubMed: 23984878]

[52]. Qiu Y-C, Yuan S, Li X-X, Du D-Y, Wang C, Qin J-S, Drake HF, Lan Y-Q, Jiang L, Zhou H-C, J. Am. Chem. Soc 141 (2019) 13841–13848. [PubMed: 31343873]

[53]. Cichocka MO, Liang Z, Feng D, Back S, Siahrostami S, Wang X, Samperisi L, Sun Y, Xu H, Hedin N, Zheng H, Zou X, Zhou H-C, Huang Z, J. Am. Chem. Soc 142 (2020) 1538–15395.

[54]. Wang K, Feng D, Liu T-F, Su J, Yuan S, Chen Y-P, Bosch M, Zou X, Zhou H-C, J. Am. Chem. Soc 136 (2014) 13983–13986. [PubMed: 25208035]

[55]. Liu Q, Cong H, Deng H, J. Am. Chem. Soc 138 (2016) 13822–13825. [PubMed: 27701854]

[56]. Wang K, Lv X-L, Feng D, Li J, Chen S, Sun J, Song L, Xie Y, Li J-R, Zhou H-C, J. Am. Chem. Soc 138 (2016) 914–919. [PubMed: 26717254]

[57]. Liu D, Liu T-F, Chen Y-P, Zou L, Feng D, Wang K, Zhang Q, Yuan S, Zhong C, Zhou H-C, J. Am. Chem. Soc 137 (2015) 7740–7746. [PubMed: 26011818]

[58]. Lu K, He C, Lin W, J. Am. Chem. Soc 136 (2014) 16712–16715. [PubMed: 25407895]

[59]. Micheroni D, Lan G, Lin W, J. Am. Chem. Soc 140 (2018) 15591–15595. [PubMed: 30392362]

[60]. Gao W-Y, Tsai C-Y, Wojtas L, Thiounn T, Lin C-C, Ma S, Inorg. Chem 55 (2016) 7291–7294. [PubMed: 27337152]

[61]. Zhao Y, Qi S, Niu Z, Peng Y, Shan C, Verma G, Wojtas L, Zhang Z, Zhang B, Feng Y, Chen Y-S, Ma S, J. Am. Chem. Soc 141 (2019) 14443–14450. [PubMed: 31431009]

[62]. Wu H, Yang F, Lv X-L, Wang B, Zhang Y-Z, Zhao M-J, Li J-R, J. Mater. Chem. A 5 (2017) 14525–14529.

[63]. Yang X-L, Xie M-H, Zou C, He Y, Chen B, O'Keeffe M, Wu C-D, J. Am. Chem. Soc 134 (2012) 10638–10645. [PubMed: 22650149]

[64]. Wang X-S, Chrzanowski M, Gao W-Y, Wojtas L, Chen Y-S, Zaworotko MJ, Ma S, Chem. Sci 3 (2012) 2823–2827.

[65]. Johnson JA, Zhang X, Reeson TC, Chen Y-S, Zhang J, J. Am. Chem. Soc 136 (2014) 15881–15884. [PubMed: 25341191]

[66]. Fasan R, ACS Catal 2 (2012) 647–666.

[67]. Nath I, Chakraborty J, Verpoort F, Chem. Soc. Rev 45 (2016) 4127–4170. [PubMed: 27251115]

[68]. Feiters MC, Rowan AE, Nolte RJM, Chem. Soc. Rev 29 (2000) 375–384.

[69]. Wiester MJ, Ulmann PA, Mirkin CA, Angew. Chem., Int. Ed 50 (2011) 114–137.

[70]. Dong Z, Luo Q, Liu J, Chem. Soc. Rev 41 (2012) 7890–7908. [PubMed: 22972005]

[71]. Wei H, Wang E, Chem. Soc. Rev 42 (2013) 6060–6093. [PubMed: 23740388]

[72]. Raynal M, Ballester P, Vidal-Ferran A, van Leeuwen PWNM, Chem. Soc. Rev 43 (2014) 1734–1787. [PubMed: 24365792]

[73]. Feng D, Jiang H-L, Chen Y-P, Gu Z-Y, Wei Z, Zhou H-C, Inorg. Chem 52 (2013) 12661–12667. [PubMed: 24147847]

[74]. Zou C, Zhang T, Xie M-H, Yan L, Kong G-Q, Yang X-L, Ma A, Wu C-D, Inorg. Chem 52 (2013) 3620–3626. [PubMed: 23517489]

[75]. Zhao M, Ou S, Wu C-D, Acc. Chem. Res 47 (2014) 1199–1207. [PubMed: 24499017]

[76]. Lv X-L, Wang K, Wang B, Su J, Zou X, Xie Y, Li J-R, Zhou H-C, J. Am. Chem. Soc 139 (2017) 211–217. [PubMed: 27936748]

[77]. Zhang L, Yuan S, Feng L, Guo B, Qin J-S, Xu B, Lollar C, Sun D, Zhou H-C, Angew. Chem., Int. Ed 57 (2018) 5095–5099.

[78]. Lin Z, Zhang Z-M, Chen Y-S, Lin W, Angew. Chem., Int. Ed 55 (2016) 13739–13743.

[79]. Zhang M, Bosch M, Gentle Iii T, Zhou H-C, CrystEngComm 16 (2014) 4069–4083.

[80]. Delgado-Friedrichs O, O'Keeffe M, Yaghi OM, Acta Crystallogr A 62 (2006) 350–355. [PubMed: 16926483]

[81]. Liu G, Cui H, Wang S, Zhang L, Su C-Y, J. Mater. Chem. A 8 (2020) 8376–8382.

[82]. Beyzavi MH, Vermeulen NA, Howarth AJ, Tussupbayev S, League AB, Schweitzer NM, Gallagher JR, Platero-Prats AE, Hafezi N, Sarjeant AA, Miller JT, Chapman KW, Stoddart JF, Cramer CJ, Hupp JT, Farha OK, J. Am. Chem. Soc 137 (2015) 13624–13631. [PubMed: 26434603]

[83]. Luo T-Y, Liu C, Eliseeva SV, Muldoon PF, Petoud S, Rosi NL, J. Am. Chem. Soc 139 (2017) 9333–9340. [PubMed: 28618777]

[84]. Victor Q-N, Hatem TM, Amy S, Ashlee H, Building a Shp: A New Rare-Earth Metal-Organic Framework and Its Application in a Catalytic Photo-Oxidation, Reaction (2020), 10.26434/chemrxiv.12355406.v1.

[85]. Gándara F, Andrés A.d., Gómez-Lor B, Gutiérrez-Puebla E, Iglesias M, Monge MA, Proserpio DM, Snejko N, Cryst. Growth Des, 8 (2008) 378–380.

[86]. Luebke R, Belmabkhout Y, Weseli ski ŁJ, Cairns AJ, Alkordi M, Norton G, Wojtas Ł, Adil K, Eddaoudi M, Chem. Sci 6 (2015) 4095–4102. [PubMed: 29218176]

[87]. Skarmoutsos I, Eddaoudi M, Maurin G, J. Phys. Chem. C 123 (2019) 26989–26999.

[88]. Xu L, Zhai M-K, Wang F, Sun L, Du H-B, Dalton Trans 45 (2016) 17108–17112. [PubMed: 27761541]

[89]. Xie M-H, Yang X-L, He Y, Zhang J, Chen B, Wu C-D, Chem. Eur. J 19 (2013) 14316–14321. [PubMed: 24038207]

[90]. Brown JW, Nguyen QT, Otto T, Jarenwattananon NN, Glöggler S, Bouchard L-S, Catal. Commun 59 (2015) 50–54.

[91]. Beyzavi MH, Vermeulen NA, Zhang K, So M, Kung C-W, Hupp JT, Farha OK, ChemPlusChem 81 (2016) 708–713. [PubMed: 31968834]

[92]. Meng L, Cheng Q, Kim C, Gao W-Y, Wojtas L, Chen Y-S, Zaworotko MJ, Zhang XP, Ma S, Angew. Chem., Int. Ed 51 (2012) 10082–10085.

[93]. Wang X-S, Chrzanowski M, Wojtas L, Chen Y-S, Ma S, Chem. Eur. J 19 (2013) 3297–3301. [PubMed: 23386517]

[94]. Zhang W, Gao W, Pham T, Jiang P, Ma S, Cryst. Growth Des. 16 (2016) 1005–1009.

[95]. Castro KADF, Figueira F, Mendes RF, Cavaleiro JAS, Neves M.d.G.P.M.S., Simões MMQ, Almeida Paz FA, Tomé JPC, Nakagaki S, ChemCatChem, 9 (2017) 2939–2945.

[96]. Zhao M, Wu C-D, ChemCatChem 9 (2017) 1192–1196.

[97]. Huang N, Wang K, Drake H, Cai P, Pang J, Li J, Che S, Huang L, Wang Q, Zhou H-C, J. Am. Chem. Soc 140 (2018) 6383–6390. [PubMed: 29719956]

[98]. Gao W-Y, Wojtas L, Ma S, Chem. Commun 50 (2014) 5316–5318.

[99]. He L, Nath JK, Lin Q, Chem. Commun 55 (2019) 412–415.

[100]. He T, Ni B, Xu X, Li H, Lin H, Yuan W, Luo J, Hu W, Wang X, Appl ACS, Mater. Interfaces 9 (2017) 22732–22738.

[101]. Wang X, Gao W-Y, Niu Z, Wojtas L, Perman JA, Chen Y-S, Li Z, Aguila B, Ma S, Chem. Commun 54 (2018) 1170–1173.

[102]. Cui H, Wang Y, Wang Y, Fan Y-Z, Zhang L, Su C-Y, CrystEngComm 18 (2016) 2203–2209.

[103]. Roy S, George CB, Ratner MA, J. Phys. Chem. C 116 (2012) 23494–23502.

[104]. Huang N, Yuan S, Drake H, Yang X, Pang J, Qin J, Li J, Zhang Y, Wang Q, Jiang D, Zhou H-C, J. Am. Chem. Soc 139 (2017) 18590–18597. [PubMed: 29172485]

[105]. So MC, Beyzavi MH, Sawhney R, Shekhah O, Eddaoudi M, Al-Juaid SS, Hupp JT, Farha OK, Chem. Commun 51 (2015) 85–88.

[106]. Majewski MB, Noh H, Islamoglu T, Farha OK, J. Mater. Chem. A 6 (2018) 7338–7350.

[107]. Cai X, Xie Z, Li D, Kassymova M, Zang S-Q, Jiang H-L, Coord. Chem. Rev 417 (2020) 213366.

[108]. Khan NA, Hasan Z, Jhung SH, Coord. Chem. Rev 376 (2018) 20–45.

[109]. Marshall CR, Staudhammer SA, Brozek CK, Chem. Sci 10 (2019) 9396–9408. [PubMed: 32055316]

[110]. Semrau AL, Stanley PM, Urstoeger A, Schuster M, Cokoja M, Fischer RA, ACS Catal 10 (2020) 3203–3211.

[111]. Lee DH, Kim S, Hyun MY, Hong J-Y, Huh S, Kim C, Lee SJ, Chem. Commun 48 (2012) 5512–5514.

[112]. Deenadayalan MS, Sharma N, Verma PK, Nagaraja CM, Inorg. Chem 55 (2016) 5320–5327. [PubMed: 27191376]

[113]. Spoerke ED, Small LJ, Foster ME, Wheeler J, Ullman AM, Stavila V, Rodriguez M, Allendorf MD, J. Phys. Chem. C 121 (2017) 4816–4824.

[114]. Liu C, Wang C, Wang H, Wang T, Jiang J, Eur. J. Inorg. Chem 2019 (2019) 4815–4819.

[115]. Wang X-S, Chen C-H, Ichihara F, Oshikiri M, Liang J, Li L, Li Y, Song H, Wang S, Zhang T, Huang Y-B, Cao R, Ye J, Appl. Catal., B 253 (2019) 323–330.

[116]. Yang Y, Ishida M, Yasutake Y, Fukatsu S, Fukakusa C, Morikawa M-A, Yamada T, Kimizuka N, Furuta H, Inorg. Chem 58 (2019) 4647–4656. [PubMed: 30875205]

[117]. Huang Z-W, Hu K-Q, Mei L, Kong X-H, Yu J-P, Liu K, Zeng L-W, Chai Z-F, Shi W-Q, Dalton Trans 49 (2020) 983–987. [PubMed: 31904068]

[118]. Liu C, Liu K, Wang C, Liu H, Wang H, Su H, Li X, Chen B, Jiang J, Nat. Commun 11 (2020) 1047. [PubMed: 32103004]

[119]. Liu J, Zhang K, Chen Z, Wei Z-W, Zhang L, Chem. - Asian J 15 (2020) 1118–1124. [PubMed: 32061120]

[120]. Gong X, Shu Y, Jiang Z, Lu L, Xu X, Wang C, Deng H, Angew. Chem., Int. Ed 59 (2020) 5326–5331.

[121]. Yuan S, Qin J-S, Zou L, Chen Y-P, Wang X, Zhang Q, Zhou H-C, J. Am. Chem. Soc 138 (2016) 6636–6642. [PubMed: 27151517]

[122]. Liu J, Zhou W, Liu J, Fujimori Y, Higashino T, Imahori H, Jiang X, Zhao J, Sakurai T, Hattori Y, Matsuda W, Seki S, Garlapati SK, Dasgupta S, Redel E, Sun L, Wöll C, J. Mater. Chem. A 4 (2016) 12739–12747.

[123]. Toyao T, Ueno N, Miyahara K, Matsui Y, Kim T-H, Horiuchi Y, Ikeda H, Matsuoka M, Chem. Commun 51 (2015) 16103–16106.

[124]. Liu J, Fan Y-Z, Li X, Wei Z, Xu Y-W, Zhang L, Su C-Y, Appl. Catal., B 231 (2018) 173–181.

[125]. Leng F, Liu H, Ding M, Lin Q-P, Jiang H-L, ACS Catal. 8 (2018) 4583–4590.

[126]. Xu H-Q, Hu J, Wang D, Li Z, Zhang Q, Luo Y, Yu S-H, Jiang H-L, J. Am. Chem. Soc 137 (2015) 13440–13443. [PubMed: 26434687]

[127]. Zhang H, Wei J, Dong J, Liu G, Shi L, An P, Zhao G, Kong J, Wang X, Meng X, Zhang J, Ye J, Angew. Chem., Int. Ed 55 (2016) 14310–14314.

[128]. Jiang ZW, Zou YC, Zhao TT, Zhen SJ, Li YF, Huang CZ, Angew. Chem., Int. Ed 59 (2020) 3300–3306.

[129]. Demel J, Kubát P, Millange F, Marrot J, Císa ová I, Lang K, Inorg. Chem 52 (2013) 2779–2786. [PubMed: 23425315]

[130]. Johnson JA, Luo J, Zhang X, Chen Y-S, Morton MD, Echeverría E, Torres FE, Zhang J, ACS Catal 5 (2015) 5283–5291.

[131]. Liu Y, Howarth AJ, Hupp JT, Farha OK, Angew. Chem., Int. Ed 54 (2015) 9001–9005.

[132]. Buru CT, Majewski MB, Howarth AJ, Lavroff RH, Kung C-W, Peters AW, Goswami S, Farha OK, Appl ACS, Mater. Interfaces 10 (2018) 23802–23806.

[133]. Yuan S, Liu T-F, Feng D, Tian J, Wang K, Qin J, Zhang Q, Chen Y-P, Bosch M, Zou L, Teat SJ, Dalgarno SJ, Zhou H-C, Chem. Sci 6 (2015) 3926–3930. [PubMed: 29218163]

[134]. Shi L, Yang L, Zhang H, Chang K, Zhao G, Kako T, Ye J, Appl. Catal., B 224 (2018) 60–68.

[135]. Wang L, Jin P, Duan S, Huang J, She H, Wang Q, An T, Environ. Sci, Nano 6 (2019) 2652–2661.

[136]. Ortega-Guerrero A, Fumanal M, Capano G, Tavernelli I, Smit B, Chem. Mater 32 (2020) 4194–4204.

[137]. Aziz A, Ruiz-Salvador AR, Hernández NC, Calero S, Hamad S, GrauCrespo R, J. Mater. Chem. A 5 (2017) (1904) 11894–11901.

[138]. Xie M-H, Yang X-L, Zou C, Wu C-D, Inorg. Chem 50 (2011) 5318–5320. [PubMed: 21568275]

[139]. Li S, Mei H-M, Yao S-L, Chen Z-Y, Lu Y-L, Zhang L, Su C-Y, Chem. Sci 10 (2019) 10577–10585. [PubMed: 32110343]

[140]. Wang X, Zhang X, Zhou W, Liu L, Ye J, Wang D, Nano Energy 62 (2019) 250–258.

[141]. Zuo Q, Liu T, Chen C, Ji Y, Gong X, Mai Y, Zhou Y, Angew. Chem., Int. Ed 58 (2019) 10198–10203.

[142]. He T, Chen S, Ni B, Gong Y, Wu Z, Song L, Gu L, Hu W, Wang X, Angew. Chem., Int. Ed 57 (2018) 3493–3498.

[143]. Sasan K, Lin Q, Mao C, Feng P, Chem. Commun 50 (2014) 10390–10393.

[144]. Wang L, Fan H, Bai F, MRS Bulletin 45 (2020) 49–56.

[145]. Liu Y, Yang Y, Sun Q, Wang Z, Huang B, Dai Y, Qin X, Zhang X, ACS Appl. Mater. Interfaces 5 (2013) 7654–7658. [PubMed: 23808795]

[146]. Sadeghi N, Sharifnia S, Sheikh Arabi M, J. CO2 Util 16 (2016) 450–457.

[147]. Chen E-X, Qiu M, Zhang Y-F, Zhu Y-S, Liu L-Y, Sun Y-Y, Bu X, Zhang J, Lin Q, Adv. Mater 30 (2018) 1704388.

[148]. Sadeghi N, Sharifnia S, Do T-O, J. Mater. Chem. A 6 (2018) 18031–18035.

[149]. Sadeghi N, Sharifnia S, Do T-O, React. Kinet., Mech. Catal, 125 (2018) 411–431.

[150]. Ye L, Gao Y, Cao S, Chen H, Yao Y, Hou J, Sun L, Appl. Catal., B 227 (2018) 54–60.

[151]. Chen L, Wang Y, Yu F, Shen X, Duan C, J. Mater. Chem. A 7 (2019) 11355–11361.

[152]. Sharma N, Dhankhar SS, Nagaraja CM, Microporous Mesoporous Mater 280 (2019) 372–378.

[153]. Wang L, Jin P, Duan S, She H, Huang J, Wang Q, Sci. Bull 64 (2019) 926–933.

[154]. Wang L, Jin P, Huang J, She H, Wang Q, ACS Sustainable Chem. Eng 7 (2019) 15660–15670.

[155]. Wu L-Y, Mu Y-F, Guo X-X, Zhang W, Zhang Z-M, Zhang M, Lu T-B, Angew. Chem., Int. Ed 58 (2019) 9491–9495.

[156]. Zheng C, Qiu X, Han J, Wu Y, Liu S, Appl ACS, Mater. Interfaces 11 (2019) 42243–42249.

[157]. Wang S-S, Huang H-H, Liu M, Yao S, Guo S, Wang J-W, Zhang Z-M, Lu T-B, Inorg. Chem 59 (2020) 6301–6307. [PubMed: 32286802]

[158]. Wang Y, Zhen W, Zeng Y, Wan S, Guo H, Zhang S, Zhong Q, J. Mater. Chem. A 8 (2020) 6034–6040.

[159]. Xu J, Liu X, Zhou Z, Xu M, Appl. Surf. Sci 513 (2020) 145801.

[160]. Zhao Y, Dong Y, Lu F, Ju C, Liu L, Zhang J, Zhang B, Feng Y, J. Mater. Chem. A 5 (2017) 15380–15389.

[161]. McKeown E, Waters WA, J. Chem. Soc. B (1966) 1040–1046.

[162]. Ogilby PR, Chem. Soc. Rev 39 (2010) 3181–3209. [PubMed: 20571680]

[163]. Zhao F-Y, Li W-J, Guo A, Chang L, Li Y, Ruan W-J, RSC Adv 6 (2016) 26199–26202.

[164]. Meng A-N, Chaihu L-X, Chen H-H, Gu Z-Y, Sci. Rep 7 (2017) 6297. [PubMed: 28740182]

[165]. Li L, Yu X, Xu L, Zhao Y, Chem. Eng. J 386 (2020) 123955.

[166]. Pereira CF, Liu Y, Howarth A, Figueira F, Rocha J, Hupp JT, Farha OK, Tomé JPC, Almeida Paz FA, A.C.S. Appl, Nano Mater 2 (2019) 465–469.

[167]. Hod I, Sampson MD, Deria P, Kubiak CP, Farha OK, Hupp JT, ACS Catal 5 (2015) 6302–6309.

[168]. Vesborg PCK, Seger B, Chorkendorff I, J. Phys. Chem. Lett 6 (2015) 951–957. [PubMed: 26262851]

[169]. Vesborg PCK, Jaramillo TF, RSC Adv 2 (2012) 7933–7947.

[170]. Nørskov JK, Bligaard T, Logadottir A, Kitchin JR, Chen JG, Pandelov S, Stimming U, J. Electrochem. Soc 152 (2005) J23.

[171]. Katz MJ, Riha SC, Jeong NC, Martinson ABF, Farha OK, Hupp JT, Coord. Chem. Rev 256 (2012) 2521–2529.

[172]. Song J, Wei C, Huang Z-F, Liu C, Zeng L, Wang X, Xu ZJ, Chem. Soc. Rev 49 (2020) 2196–2214. [PubMed: 32133479]

[173]. Tahir M, Pan L, Idrees F, Zhang X, Wang L, Zou J-J, Wang ZL, Nano Energy 37 (2017) 136–157.

[174]. Subbaraman R, Tripkovic D, Chang K-C, Strmcnik D, Paulikas AP, Hirunsit P, Chan M, Greeley J, Stamenkovic V, Markovic NM, Nat. Mater 11 (2012) 550–557. [PubMed: 22561903]

[175]. Sultan S, Tiwari JN, Singh AN, Zhumagali S, Ha M, Myung CW, Thangavel P, Kim KS, Adv. Energy Mater 9 (2019) 1900624.

[176]. Kellett RM, Spiro TG, Inorg. Chem 24 (1985) 2378–2382.

[177]. Beyene BB, Mane SB, Hung C-H, Chem. Commun 51 (2015) 15067–15070.

[178]. Usov PM, Ahrenholtz SR, Maza WA, Stratakes B, Epley CC, Kessinger MC, Zhu J, Morris AJ, J. Mater. Chem. A 4 (2016) 16818–16823.

[179]. Fletcher S, J. Solid State Electrochem 13 (2009) 537–549.

[180]. McGrath DT, Ryan MD, MacInnis JJ, VandenBoer TC, Young CJ, Katz MJ, Chem. Sci 10 (2019) 5576–5581. [PubMed: 31293741]

[181]. Katz MJ, Klet RC, Moon S-Y, Mondloch JE, Hupp JT, Farha OK, ACS Catal 5 (2015)4637–4642.

[182]. Sohrabi S, Dehghanpour S, Ghalkhani M, J. Mater. Sci 53 (2018) 3624–3639.

[183]. Dai F, Fan W, Bi J, Jiang P, Liu D, Zhang X, Lin H, Gong C, Wang R, Zhang L, Sun D, Dalton Trans 45 (2016) 61–65. [PubMed: 26606194]

[184]. Meng J, Zhou Y, Chi H, Li K, Wan J, Hu Z, ChemistrySelect 4 (2019) 8661–8670.

[185]. Yoshikawa S, Shimada A, Chem. Rev 115 (2015) 1936–1989. [PubMed: 25603498]

[186]. Shao M, Chang Q, Dodelet J-P, Chenitz R, Chem. Rev 116 (2016) 3594–3657. [PubMed: 26886420]

[187]. Sinha S, Ghosh M, Warren JJ, ACS Catal 9 (2019) 2685–2691.

[188]. Jahan M, Bao Q, Loh KP, J. Am. Chem. Soc 134 (2012) 6707–6713. [PubMed: 22439970]

[189]. Sohrabi S, Dehghanpour S, Ghalkhani M, ChemCatChem 8 (2016) 2356–2366.

[190]. Usov PM, Huffman B, Epley CC, Kessinger MC, Zhu J, Maza WA, Morris AJ, A.C.S. Appl, Mater. Interfaces 9 (2017) 33539–33543.

[191]. Coleman EJ, Chowdhury MH, Co AC, ACS Catal 5 (2015) 1245–1253.

[192]. Costentin C, Robert M, Savéant J-M, Acc. Chem. Res 48 (2015) 2996–3006. [PubMed: 26559053]

[193]. Qiao J, Liu Y, Hong F, Zhang J, Chem. Soc. Rev 43 (2014) 631–675. [PubMed: 24186433]

[194]. Costentin C, Drouet S, Robert M, Savéant J-M, Science 338 (2012) 90. [PubMed: 23042890]

[195]. Dong B-X, Qian S-L, Bu F-Y, Wu Y-C, Feng L-G, Teng Y-L, Liu W-L, Li Z-W, ACS Appl. Energy Mater 1 (2018) 4662–4669.

[196]. Wu J-X, Hou S-Z, Zhang X-D, Xu M, Yang H-F, Cao P-S, Gu Z-Y, Chem. Sci 10 (2019) 2199–2205. [PubMed: 30881645]

[197]. Kornienko N, Zhao Y, Kley CS, Zhu C, Kim D, Lin S, Chang CJ, Yaghi OM, Yang P, J. Am. Chem. Soc 137 (2015) 14129–14135. [PubMed: 26509213]

[198]. Yin D, Liu J, Bo X, Li M, Guo L, Electrochim. Acta 247 (2017) 41–49.

[199]. Li H-Y, Zhao S-N, Zang S-Q, Li J, Chem. Soc. Rev 49 (2020) 6364–6401. [PubMed: 32749390]

[200]. Kovacic P, Somanathan R, J. Appl. Toxicol 34 (2014) 810–824. [PubMed: 24532466]

[201]. Tchounwou PB, Yedjou CG, Patlolla AK, Sutton DJ, Experientia Supplementum 101 (2012) (2012) 133–164.

[202]. Nicolopoulou-Stamati P, Maipas S, Kotampasi C, Stamatis P, Hens L, Front. Pub. Health 4 (2016) 148. [PubMed: 27486573]

[203]. Yang J, Wang Z, Hu K, Li Y, Feng J, Shi J, Gu J, ACS Appl. Mater. Interfaces 7 (2015) (1964) 11956–11961. [PubMed: 25988802]

[204]. Pereira CF, Figueira F, Mendes RF, Rocha J, Hupp JT, Farha OK, Simões MMQ, Tomé JPC, Paz FAA, Inorg. Chem 57 (2018) 3855–3864. [PubMed: 29533608]

[205]. Zhang Y, Zhang X, Lyu J, Otake K-I, Wang X, Redfern LR, Malliakas CD, Li Z, Islamoglu T, Wang B, Farha OK, J. Am. Chem. Soc 140 (2018) 11179–11183. [PubMed: 30113833]

[206]. Ye Y, Huang C, Yang J, Li Y, Zhuang Q, Gu J, Microporous Mesoporous Mater 284 (2019) 36–42.

[207]. Wang L, He K, Quan H, Wang X, Wang Q, Xu X, Microchem. J 153 (2020) 104441.

[208]. Liu J, Xiong WH, Ye LY, Zhang WS, Yang H, Agric. J. Food Chem 68 (2020) 5572–5578.

[209]. Qiao M, Wang G-P, Zhang C, Roelofs D, van Straalen NM, Zhu Y-G, Environ. Toxicol. Chem 34 (2015) 1362–1368. [PubMed: 25703271]

[210]. Chen J, Chen H, Wang T, Li J, Wang J, Lu X, Anal. Chem. 91 (2019) 4331–4336. [PubMed: 30854846]

[211]. Chen Y-Z, Jiang H-L, Chem. Mater. 28 (2016) 6698–6704.

[212]. Yang J, Wang Z, Li Y, Zhuang Q, Zhao W, Gu J, RSC Adv 6 (2016) 69807–69814.

[213]. Moradi E, Rahimi R, Safarifard V, J. Solid State Chem 286 (2020) 121277.

[214]. Wang X.-S.e.a., Appl. Catal., B, 253 (2019) 323–330.

[215]. Hibbard HAJ, Burnley MJ, Rubin HN, Miera JA, Reynolds MM, Inorg. Chem. Commun 115 (2020) 107861.

[216]. Moradi E, Rahimi R, Farahani YD, Safarifard V, J. Solid State Chem 282 (2020) 121103.

[217]. Cheng C, Zhang R, Wang J, Zhang Y, Xiong S-S, Huang Y, Yang M, A.C.S. Appl, Mater. Interfaces 12 (2020) 26391–26398.

[218]. Kung C-W, Chang T-H, Chou L-Y, Hupp JT, Farha OK, Ho K-C, Electrochem. Commun 58 (2015) 51–56.

[219]. Wang Q-H, Yu L-J, Liu Y, Lin L, Lu R-G, Zhu J-P, He L, Lu Z-L, Talanta 165 (2017) 709–720. [PubMed: 28153321]

[220]. Kung C-W, Chang T-H, Chou L-Y, Hupp JT, Farha OK, Ho K-C, Chem. Commun 51 (2015) 2414–2417.

[221]. Kung C-W, Li Y-S, Lee M-H, Wang S-Y, Chiang W-H, Ho K-C, J. Mater. Chem. A 4 (2016) 10673–10682.

[222]. Zhao Y, Jiang L, Shangguan L, Mi L, Liu A, Liu S, J. Mater. Chem. A 6 (2018) 2828–2833.

[223]. Deibert BJ, Li J, Chem. Commun 50 (2014) 9636–9639.

[224]. Chen H, Wang J, Shan D, Chen J, Zhang S, Lu X, Anal. Chem 90 (2018) 7056–7063. [PubMed: 29724095]

[225]. Ling P, Lei J, Zhang L, Ju H, Anal. Chem 87 (2015) 3957–3963. [PubMed: 25741988]

[226]. Sun Y, Jin H, Jiang X, Gui R, Sens. Actuators, B 309 (2020) 127777.

[227]. Cheng H, Liu Y, Hu Y, Ding Y, Lin S, Cao W, Wang Q, Wu J, Muhammad F, Zhao X, Zhao D, Li Z, Xing H, Wei H, Anal. Chem 89 (2017) 11552–11559. [PubMed: 28992698]

[228]. Qiu Z, Yang T, Gao R, Jie G, Hou W, J. Electroanal. Chem 835 (2019) 123–129.

[229]. Ling P, Lei J, Ju H, Biosens. Bioelectron 71 (2015) 373–379. [PubMed: 25950931]

[230]. Lin Y, Sun Y, Dai Y, Sun W, Zhu X, Liu H, Han R, Gao D, Luo C, Wang X, Talanta 207 (2020) 120300. [PubMed: 31594586]

[231]. Aghayan M, Mahmoudi A, Sohrabi S, Dehghanpour S, Nazari K, Mohammadian-Tabrizi N, Anal. Methods 11 (2019) 3175–3187.

[232]. Ilacas GC, Basa A, Nelms KJ, Sosa JD, Liu Y, Gomez FA, Anal. Chim. Acta 1055 (2019) 74–80. [PubMed: 30782373]

[233]. Du P, Niu Q, Chen J, Chen Y, Zhao J, Lu X, Anal. Chem 92 (2020) 7980–7986. [PubMed: 32366095]

[234]. Wei M, Geng X, Liu Y, Long H, Du J, J. Electroanal. Chem 842 (2019) 184–192.

[235]. Liu Q, Gao J, Zheng Z, Ning D, Wang Q, Du X-M, Zhao B, Ruan W-J, Li Y, Talanta 203 (2019) 248–254. [PubMed: 31202334]

[236]. Zhang G, Shan D, Dong H, Cosnier S, Al-Ghanim KA, Ahmad Z, Mahboob S, Zhang X, Anal. Chem 90 (2018) 12284–12291. [PubMed: 30234968]

[237]. Chen K, Xue J, Zhou Q, Zhang Y, Zhang M, Zhang Y, Zhang H, Shen Y, Anal. Chim. Acta 1107 (2020) 145–154. [PubMed: 32200889]

[238]. Zhang G-Y, Cai C, Cosnier S, Zeng H-B, Zhang X-J, Shan D, Nanoscale 8 (2016) 11649–11657. [PubMed: 27218308]

[239]. Zhang G, Chai H, Tian M, Zhu S, Qu L, Zhang X, Anal. Chem 92 (2020) 7354–7362. [PubMed: 32319281]

[240]. Ling P, Qian C, Yu J, Gao F, Biosens. Bioelectron 149 (2020) 111838. [PubMed: 31739109]

[241]. Ling P, Lei J, Ju H, Anal. Chem 88 (2016) 10680–10686. [PubMed: 27728765]

[242]. Xu R.e.a., J. Am. Chem. Soc, 138 (2016) 2158–2161. [PubMed: 26864385]

[243]. Ye Y, Liu H, Li Y, Zhuang Q, Liu P, Gu J, Talanta 200 (2019) 472–479. [PubMed: 31036211]

[244]. Liu J, Bo X, Yang J, Yin D, Guo L, Sens. Actuators, B 248 (2017) 207–213.

[245]. Ma Y, Su H, Kuang X, Li X, Zhang T, Tang B, Anal. Chem 86 (2014) 11459–11463. [PubMed: 25342497]

[246]. Ou DS, Duanping Liang, Zhixian Chen, Bowen Lin, Xiangan' Chen Zuanguang, Sens. Actuators, B, 285 (2019) 398–404.

[247]. Agarwal PK, Microb. Cell Fact 5 (2006) 2. [PubMed: 16409630]

[248]. Lemmon MA, Schlessinger J, Cell 141 (2010) 1117–1134. [PubMed: 20602996]

[249]. Cho H, Mu J, Kim JK, Thorvaldsen JL, Chu Q, Crenshaw EB 3rd, Kaestner KH, Bartolomei MS, Shulman GI, Birnbaum MJ, Science 292 (2001) 1728–1731. [PubMed: 11387480]

[250]. Cohen P, Nat Rev Drug Discov 1 (2002) 309–315. [PubMed: 12120282]

[251]. Xie Y, Xu M, Wang L, Liang H, Wang L, Song Y, Mater. Sci. Eng. C112 (2020) 110864.

[252]. Harris AL, Nat. Rev. Cancer 2 (2002) 38–47. [PubMed: 11902584]

[253]. Mustafa AK, Gadalla MM, Snyder SH, Sci. Signaling, 2 (2009) re2–re2.

[254]. Wang R, The FASEB Journal 16 (2002) 1792–1798. [PubMed: 12409322]

[255]. Trachootham D, Alexandre J, Huang P, Nat. Rev. Drug Discovery 8 (2009) 579–591. [PubMed: 19478820]

[256]. Kamoun P, Belardinelli MC, Chabli A, Lallouchi K, Chadefaux-Vekemans B, Am J Med Genet A, 116a (2003) 310–311. [PubMed: 12503113]

[257]. Eto K, Asada T, Arima K, Makifuchi T, Kimura H, Biochem. Biophys. Res. Commun 293 (2002) 1485–1488. [PubMed: 12054683]

[258]. Dolmans DEJGJ, Fukumura D, Jain RK, Nat. Rev. Cancer 3 (2003) 380–387. [PubMed: 12724736]

[259]. dos Santos AF, de Almeida DRQ, Terra LF, Baptista MS, Labriola L, J. Cancer Treat. Metathesis 5 (2019) 1–20.

[260]. Lismont M, Dreesen L, Wuttke S, Adv. Funct. Mater 27 (2017) 1606314.

[261]. Lu K, Aung T, Guo N, Weichselbaum R, Lin W, Adv. Mater 30 (2018) 1707634.

[262]. Lan G, Ni K, Lin W, Coord. Chem. Rev 379 (2019) 65–81. [PubMed: 30739946]

[263]. Notman N, Proc Natl Acad Sci U S A 116 (2019) 6513–6516. [PubMed: 30943662]

[264]. https://clinicaltrials.gov/ct2/show/NCT03444714, in.

[265]. Lu K, He C, Lin W, J. Am. Chem. Soc 137 (2015) 7600–7603. [PubMed: 26068094]

[266]. Park J, Jiang Q, Feng D, Mao L, Zhou H-C, J. Am. Chem. Soc 138 (2016) 3518–3525. [PubMed: 26894555]

[267]. He L, Brasino M, Mao C, Cho S, Park W, Goodwin AP, Cha JN, Small 13 (2017) 1700504.

[268]. Ma Y, Li X, Li A, Yang P, Zhang C, Tang B, Angew. Chem., Int. Ed 56 (2017) 13752–13756.

[269]. Zeng J-Y, Wang X-S, Zhang M-K, Li Z-H, Gong D, Pan P, Huang L, Cheng S-X, Cheng H, Zhang X-Z, ACS Appl. Mater. Interfaces 9 (2017) 43143–43153. [PubMed: 29168377]

[270]. Zhang Y, Wang F, Liu C, Wang Z, Kang L, Huang Y, Dong K, Ren J, Qu X, ACS Nano 12 (2018) 651–661. [PubMed: 29290107]

[271]. Zhao X, Zhang Z, Cai X, Ding B, Sun C, Liu G, Hu C, Shao S, Pang M, A.C.S. Appl, Mater. Interfaces 11 (2019) 7884–7892.

[272]. Wang C, Volotskova O, Lu K, Ahmad M, Sun C, Xing L, Lin W, J. Am. Chem. Soc 136 (2014) 6171–6174. [PubMed: 24730683]

[273]. Liu J, Yang Y, Zhu W, Yi X, Dong Z, Xu X, Chen M, Yang K, Lu G, Jiang L, Liu Z, Biomaterials 97 (2016) 1–9. [PubMed: 27155362]

[274]. Li B, Wang X, Chen L, Zhou Y, Dang W, Chang J, Wu C, Theranostics 8 (2018) 4086–4096. [PubMed: 30128038]

[275]. Wang C, Cao F, Ruan Y, Jia X, Zhen W, Jiang X, Angew. Chem., Int. Ed 58 (2019) 9846–9850.

[276]. Ni K, Aung T, Li S, Fatuzzo N, Liang X, Lin W, Chem 5 (2019) 1892–1913. [PubMed: 31384694]

[277]. Li Y, Gao Z, Chen F, You C, Wu H, Sun K, An P, Cheng K, Sun C, Zhu X, Sun B, A.C.S. Appl, Mater. Interfaces 10 (2018) 30930–30935.

[278]. Ning W, Di Z, Yu Y, Zeng P, Di C, Chen D, Kong X, Nie G, Zhao Y, Li L, Small 14 (2018) 1703812.

[279]. Wang S, Chen Y, Wang S, Li P, Mirkin CA, Farha OK, J. Am. Chem. Soc 141 (2019) 2215–2219. [PubMed: 30669839]

[280]. Chen Y, Li P, Modica JA, Drout RJ, Farha OK, J. Am. Chem. Soc 140 (2018) 5678–5681. [PubMed: 29641892]

[281]. Deria P, Bury W, Hupp JT, Farha OK, Chem. Commun 50 (2014) 19651968.

[282]. Wang S, McGuirk CM, Ross MB, Wang S, Chen P, Xing H, Liu Y, Mirkin CA, J. Am. Chem. Soc 139 (2017) 9827–9830. [PubMed: 28718644]

[283]. Li S-Y, Cheng H, Xie B-R, Qiu W-X, Zeng J-Y, Li C-X, Wan S-S, Zhang L, Liu W-L, Zhang X-Z, ACS Nano 11 (2017) 7006–7018. [PubMed: 28665106]

[284]. Li Y, Di Z, Gao J, Cheng P, Di C, Zhang G, Liu B, Shi X, Sun L-D, Li L, Yan C-H, J. Am. Chem. Soc 139 (2017) 13804–13810. [PubMed: 28899098]

[285]. Chen Z-X, Liu M-D, Zhang M-K, Wang S-B, Xu L, Li C-X, Gao F, Xie B-R, Zhong Z-L, Zhang X-Z, Adv. Funct. Mater 28 (2018) 1803498.

[286]. Lan G, Ni K, Xu Z, Veroneau SS, Song Y, Lin W, J. Am. Chem. Soc 140 (2018) 5670–5673. [PubMed: 29665677]

[287]. Lu K, He C, Guo N, Chan C, Ni K, Lan G, Tang H, Pelizzari C, Fu Y-X, Spiotto MT, Weichselbaum RR, Lin W, Nat. Biomed. Eng 2 (2018) 600–610. [PubMed: 31015630]

[288]. Zeng J-Y, Zou M-Z, Zhang M, Wang X-S, Zeng X, Cong H, Zhang X-Z, ACS Nano 12 (2018) 4630–4640. [PubMed: 29584395]

[289]. Wan S-S, Zeng J-Y, Cheng H, Zhang X-Z, Biomaterials 185 (2018) 51–62. [PubMed: 30218836]

[290]. Zeng J-Y, Zhang M-K, Peng M-Y, Gong D, Zhang X-Z, Adv. Funct. Mater 28 (2018) 1705451.

[291]. Ni K, Lan G, Chan C, Duan X, Guo N, Veroneau SS, Weichselbaum RR, Lin W, Matter 1 (2019) 1331–1353. [PubMed: 32832885]

[292]. Ni K, Lan G, Song Y, Hao Z, Lin W, Chem. Sci 11 (2020) 7641–7653.

[293]. Ni K, Luo T, Lan G, Culbert A, Song Y, Wu T, Jiang X, Lin W, Angew. Chem., Int. Ed 59 (2020) 1108–1112.

[294]. Liu W, Wang Y-M, Li Y-H, Cai S-J, Yin X-B, He X-W, Zhang Y-K, Small 13 (2017) 1603459.

[295]. Kalbasi A, Ribas A, Nat. Rev. Immunol 20 (2020) 25–39. [PubMed: 31570880]

[296]. Lu K, He C, Guo N, Chan C, Ni K, Weichselbaum RR, Lin W, J. Am. Chem. Soc 138 (2016) 12502–12510. [PubMed: 27575718]

[297]. Feng L, Wang Y, Yuan S, Wang K-Y, Li J-L, Day GS, Qiu D, Cheng L, Chen W-M, Madrahimov ST, Zhou H-C, ACS Catal 9 (2019) 5111–5118.
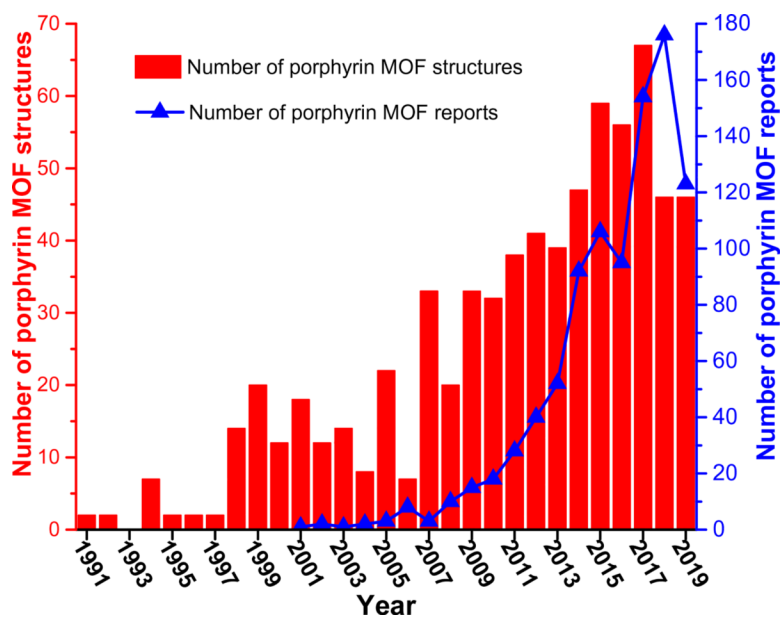
Fig. 1.

Numbers of porphyrin MOF reports found in Web of Science, and porphyrin MOF structures in the Cambridge Structural Database (CSD) from 1991 to 2019. The structural data was obtained from the MOF subset of CSD as of May 2020.
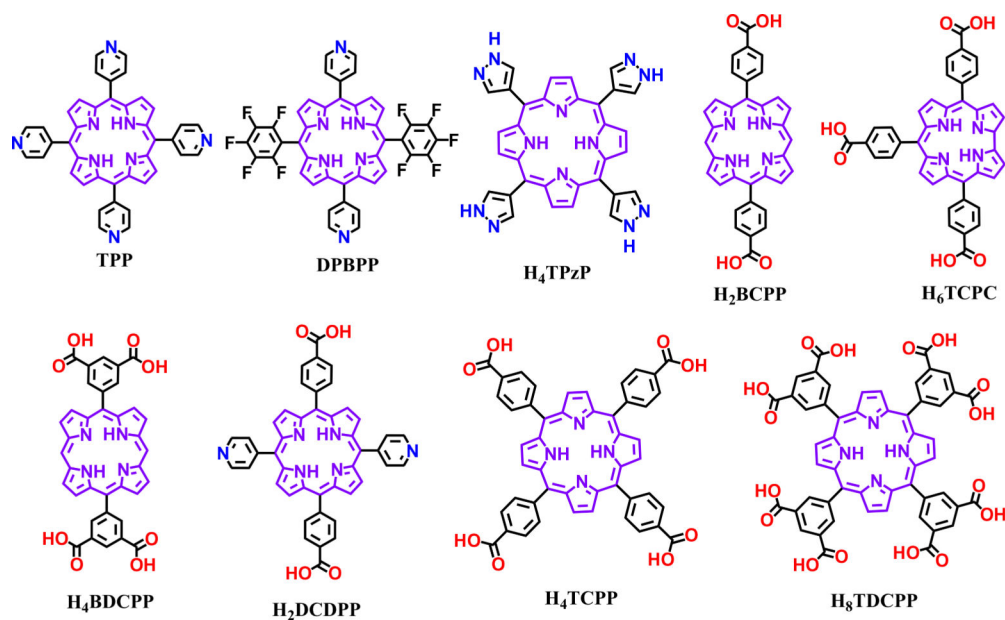
Fig. 2.
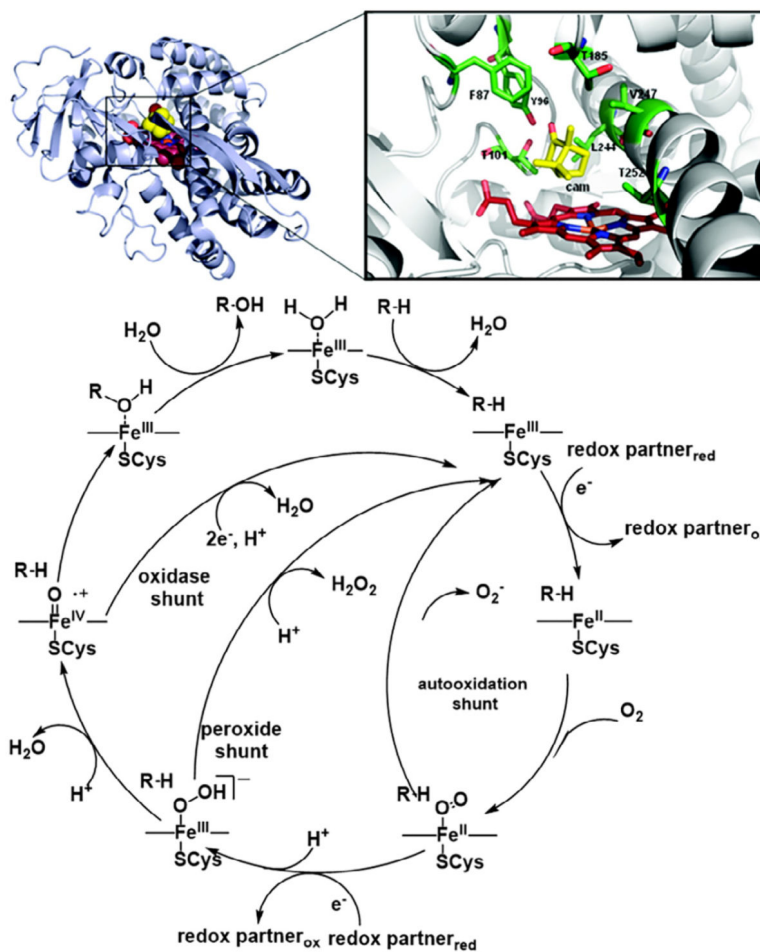Representative molecular structures of porphyrin-based organic linkers for the synthesis of MOFs.

Fig. 3.
Active site (top) and representative catalytic oxidation mechanism (bottom) of cytochrome P450. Adapted with permission from Ref. 67. Copyright 2012 American Chemical Society.
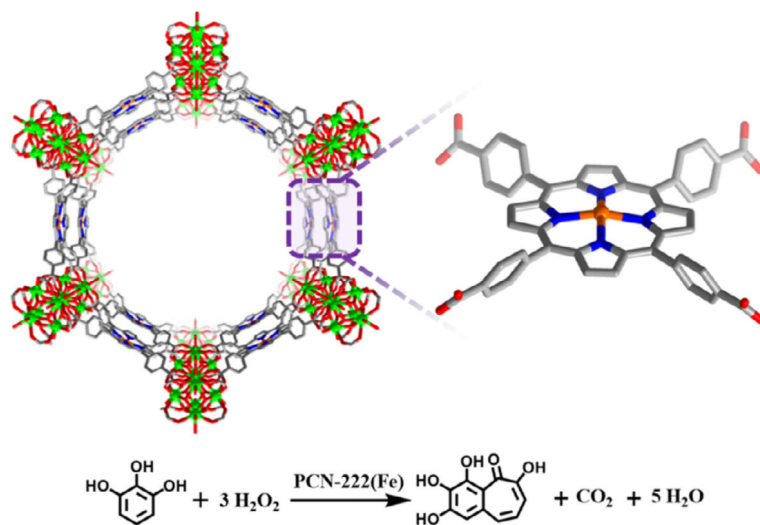
Fig. 4.
The structure of PCN-222/MOF-545 featuring iron porphyrin sites for catalyzing the oxidation of pyrogallol.
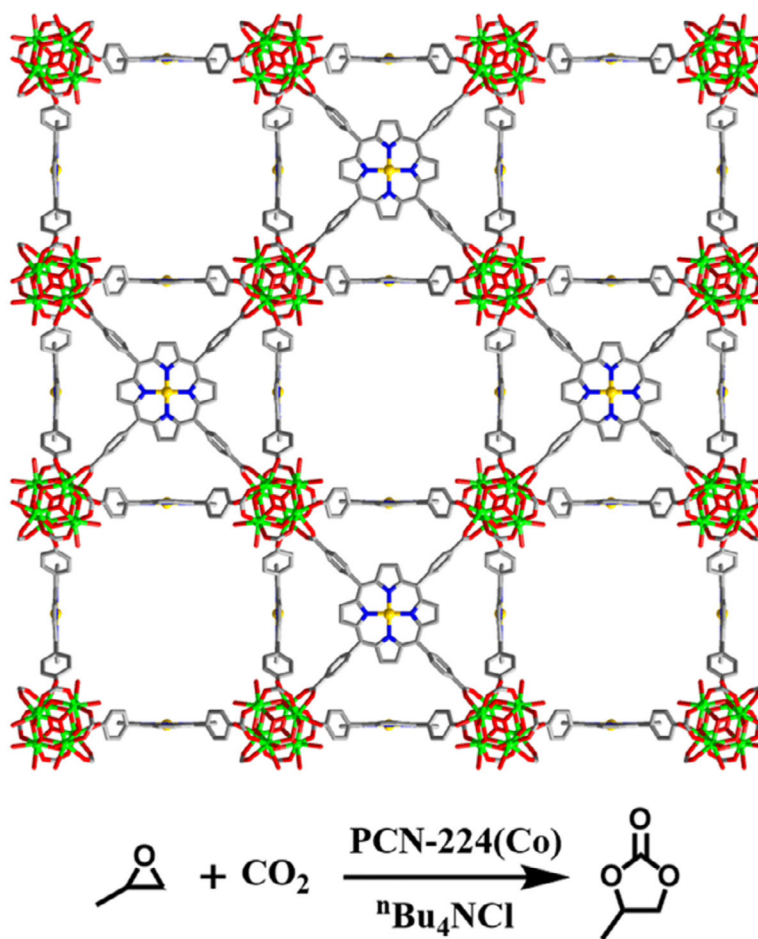
Fig. 5.
The structure of PCN-224 featuring cobalt porphyrin sites for catalyzing CO_2 insertion into expoxide.
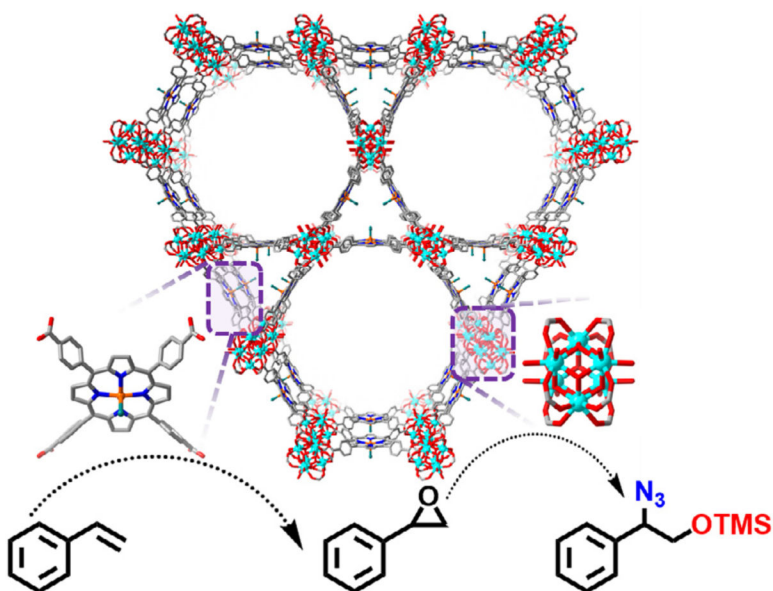
Fig. 6.
The structure of Hf-PCN-222(Fe) featuring Fe-porphyrin and Hf_6 sites for the tandem transformation of styrene.
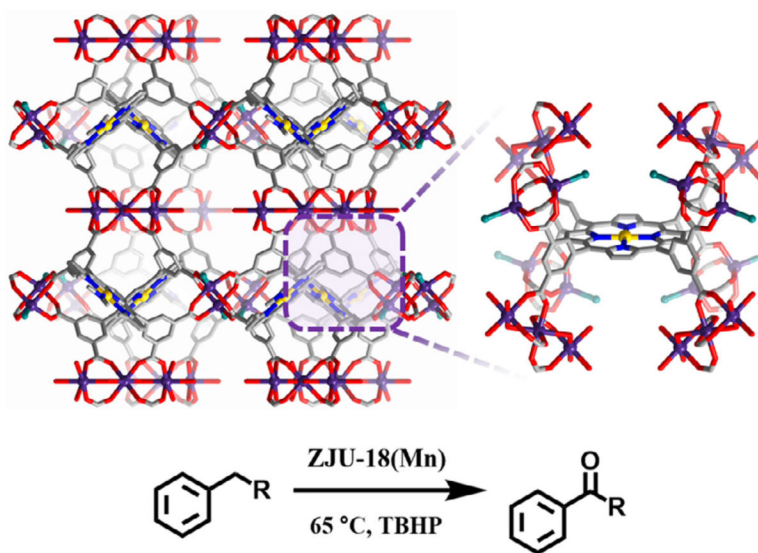
Fig. 7.
Structure of ZJU-18 featuring Mn-nodes and Mn-porphyrin linker sites for the catalytic oxidation of alkylbenzene to ketones.
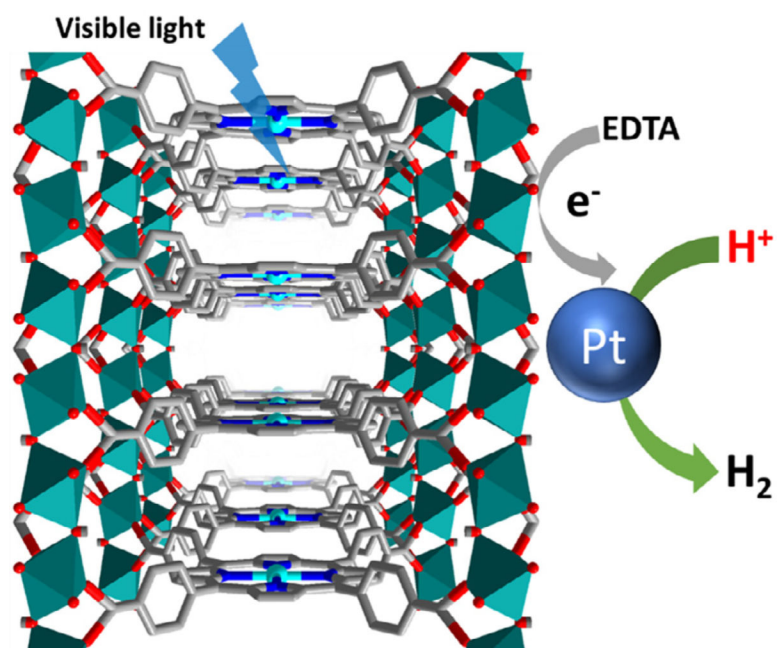
Fig. 8.
The structure of Al-PMOF featuring Zn-porphyrin sites as photosensitizers for hydrogen evolution.
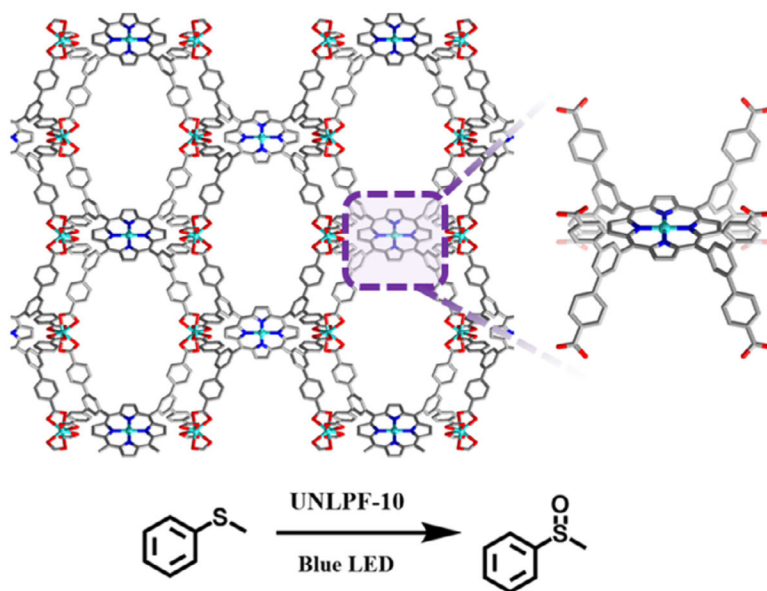
Fig. 9.
Structure of UNLPF-10 featuring In-porphyrin sites for the photocatalytic oxidation of thioanisole.
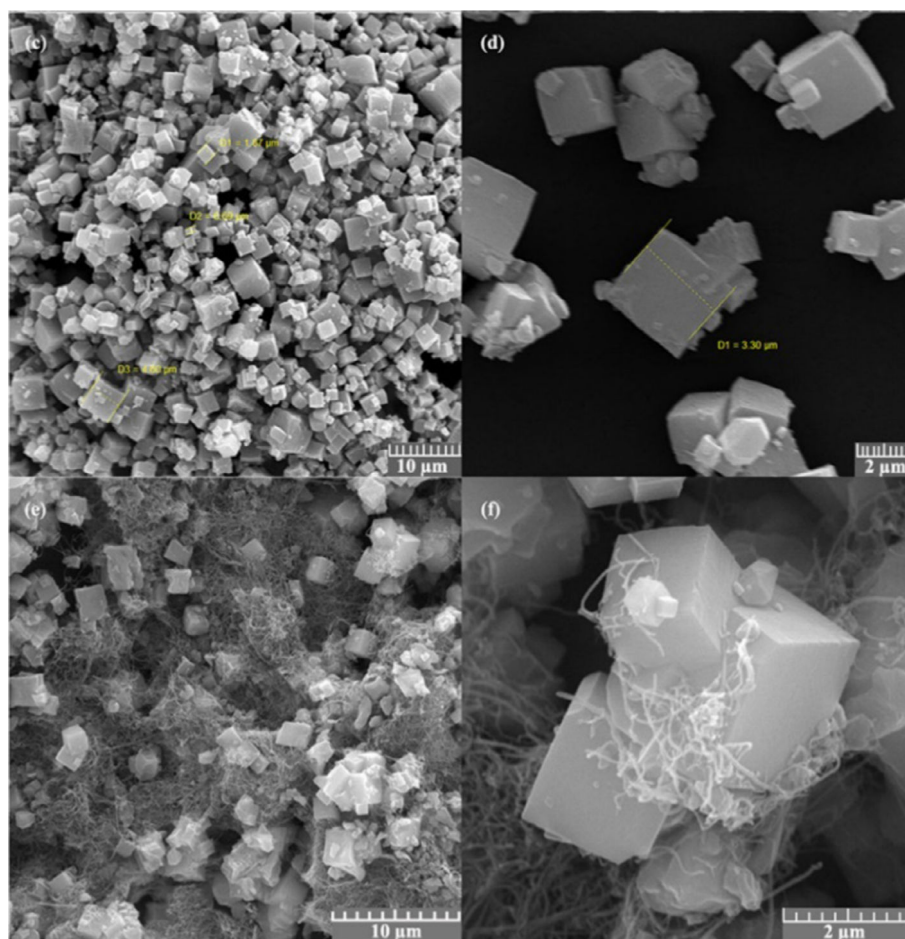
Fig. 10.
SEM images of PCN-224(Co) (top) and PCN-224(Co)/MWCNT (bottom). Adapted with permission from ref. 183. Copyright 2018 Springer Nature.
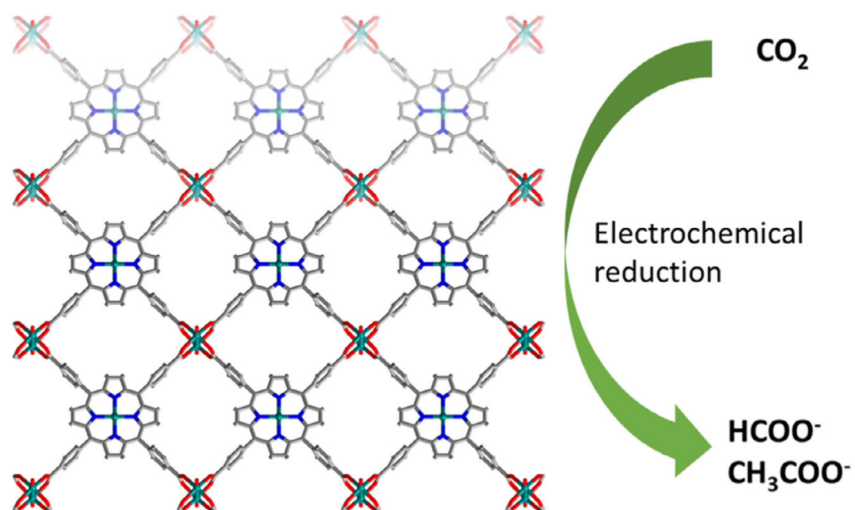
Fig. 11.
Structure of $Cu_2(CuTCPP)$ featuring Cu_2 nodes and Cu-porphyrin sites for the electrochemical reduction of CO_2 to formate and acetate.
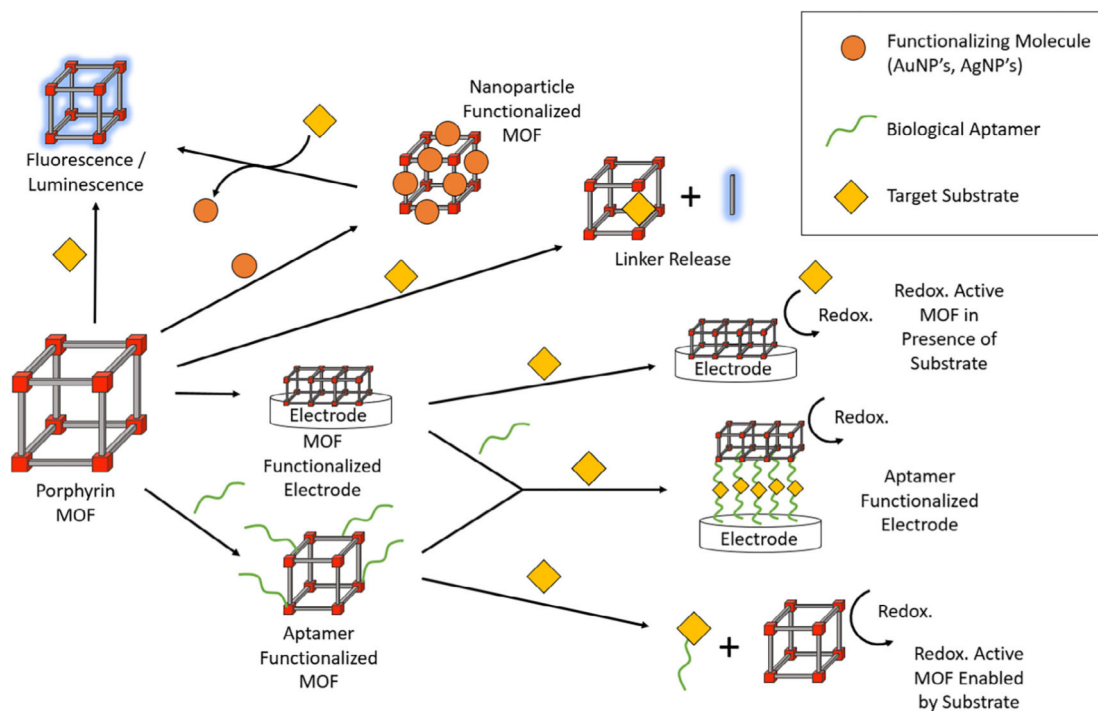
Fig. 12.
A summary of various kinds of sensing mechanisms enabled by porphyrin-based MOFs.
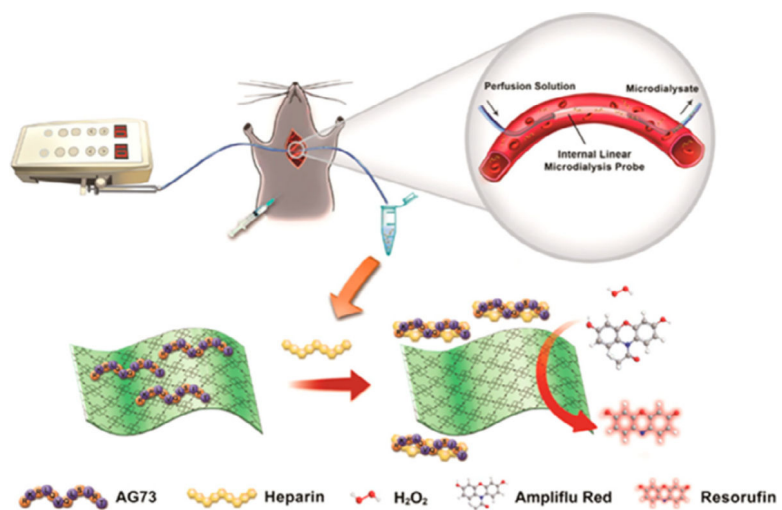
Fig. 13.
Schematic illustration of the sensing of heparin elimination process in live rats using a 2D nanosheet MOF (Zn-TCPP(Fe)). Adapted with permission from ref. 228. Copyright 2017 American Chemical Society.
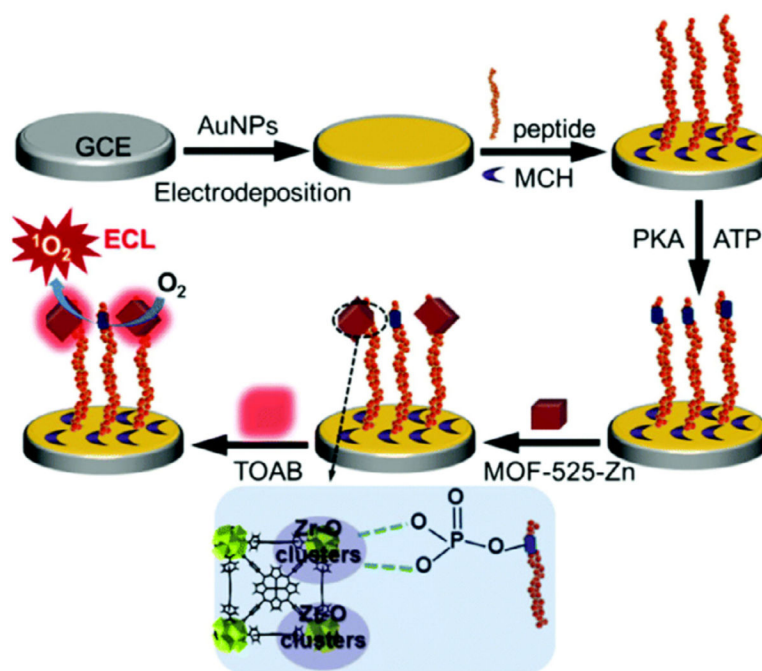
Fig. 14.
Schematic illustration of the electrochemiluminescence kinase activity assay using MOF-525 featuring Zn-porphyrin sites. Reproduced with permission from ref. 239. Copyright 2016 Royal Society of Chemistry.
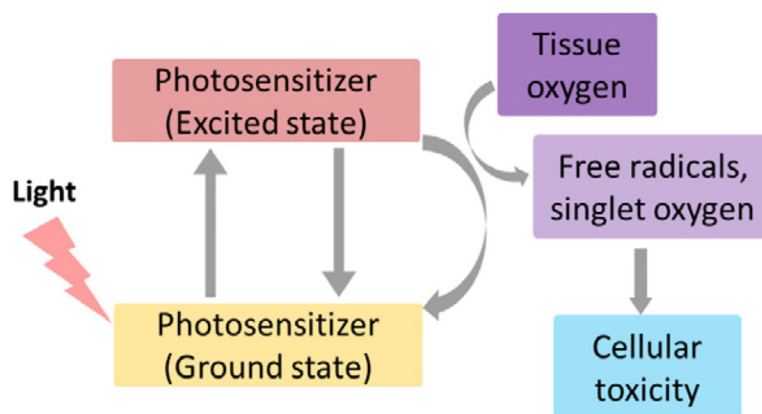
Fig. 15.
A schematic representation of PDT.
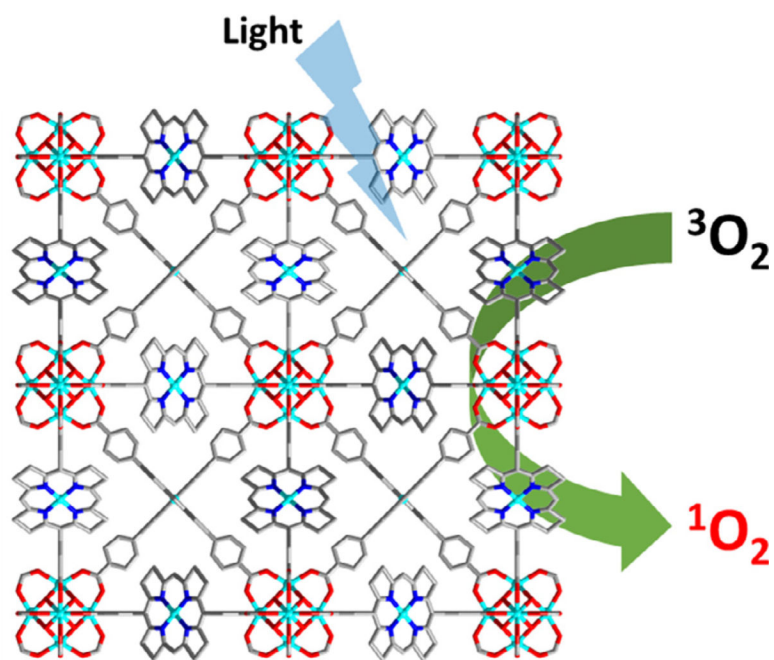
Fig. 16.
The structure of DBP-UiO featuring Hf_6 nodes and porphyrin linkers for the light induced generation of singlet oxygen.
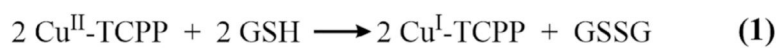
$$2\ Cu^{II}\text{-}TCPP\ +\ 2\ GSH\ \longrightarrow\ 2\ Cu^{I}\text{-}TCPP\ +\ GSSG \qquad (1)$$

$$Cu^{I}\text{-}TCPP\ +\ O_2\ \longrightarrow\ Cu^{II}\text{-}TCPP\ +\ O_2{}^{\bullet-} \qquad (2)$$

$$Cu^{I}\text{-}TCPP\ +\ H_2O_2\ \longrightarrow\ Cu^{II}\text{-}TCPP\ +\ {}^{\bullet}OH\ +\ OH^- \qquad (3)$$

$$O_2{}^{\bullet-}\ +\ H_2O\ \longrightarrow\ {}^{1}O_2\ +\ H_2O_2\ +\ 2\ OH^- \qquad (4)$$
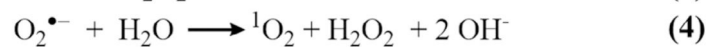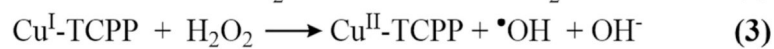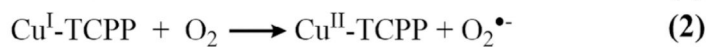
Fig. 17.
A proposed mechanism for the production of $^{1}O_2$ from Cu-TCPP in the absence of externally applied light. Here GSH is glutathione and GSSG is the oxidized form of glutathione.
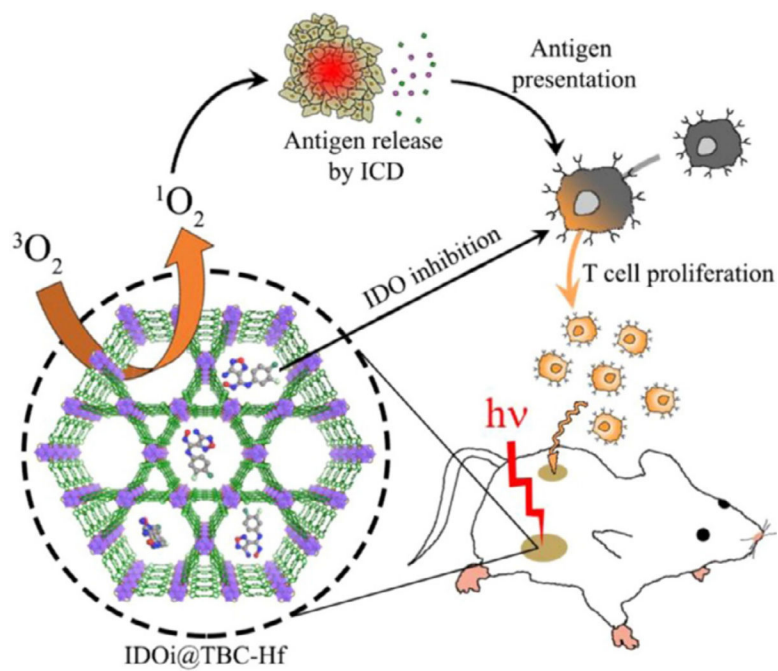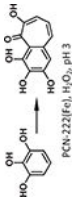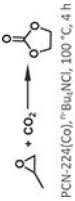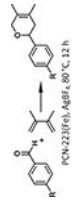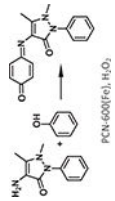
Fig. 18.
An example of utilizing a MOF (IDOi@TBC-Hf) for synergistic PDT/CBI therapy. Here the CBI therapy (IDOi) is loaded into the pores of TBC-Hf and released upon injection.
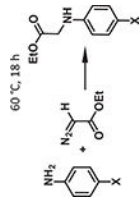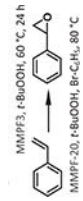Reproduced with permission from ref 297. Copyright 2016, American Chemical Society.

Table 1

Oxidation reactions of various metalloporphyrin MOFs.

Entry	Ref.	MOF	Linker	Metal Node	Porphyrin Centre	Model Reaction Conditions	Yield (%)
1	[46]	PCN-222	Fe-TCPP	$Zr_6O_4OH_4(COO^-)_8(OH)_4(H_2O)_4$	Fe		–
2	[50]	PCN-224	M-TCPP-Cl	$Zr_6O_4OH_4(COO^-)_6(OH)_6(H_2O)_6$	Ni, Co, Fe		42
3	[48]	PCN-223	TCPP	$Zr_6O_4OH_4(COO^-)_{12}$	Fe		99
4	[54]	PCN-600	M-TCPP	$Fe_3O(COO^-)_6OH$	Mn, Fe, Co, Ni, Cu		–
5	[81]	Fe-PMOF-3	Fe-TCPP	$[Fe(OH)O_4]_n^{6+}$	Fe		61
6	[82]	Hf-PCN-222	Fe-TCCP-Cl	$Hf_6O_4OH_4(COO^-)_8(OH)_4(H_2O)_4$	Fe		90
7	[88]	NUPF-2Y	TCPP	$[Y_9OH_{12}O_2(COO^-)_{12}]^-$	Fe		96
8	[92]	MMPF-3	Co-dcdbp	$[Co_2(\mu_2\text{-}H_2O)(H_2O)_4]_3(COO^-)_{12}$	Co		95.7
9	[94]	MMPF-20	Ni-dcdbp	$[Ni_3(COO^-)_8]^+$	Ni		55
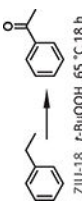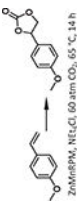
Entry	Ref.	MOF	Linker	Metal Node	Porphyrin Centre	Model Reaction Conditions	Yield (%)
10	[63]	ZJU-18	Mn-OCPP	$[Mn_5Cl_2(COO^-)_4]^{9+}$	Mn	ZJU-18, t-BuOOH, 65 °C, 18 h	>99
11	[78]	In-Co(TBP)-MOF	In-TBP, Co-TBP	$[In(COO^-)_4]^-$	In-Co	In-Co[TBP]-MOF, MeOH, 80 °C, 20 h	100
12	[91]	ZnMnRPM	Zn-TCPP,*Mn-porphyrin-Cl*	$Zn_4O(COO^-)_6$	Zn-Mn	ZnMnRPM, NEt$_4$Cl, 60 atm CO$_2$, 65 °C, 14 h	>60

Table 2

Oxygen evolution reaction performance of porphyrin MOFs.

MOF electrocatalyst	Over potential (η, V)	Current density (mA/cm^2)	Electrolyte	pH	Ref.
PCN-224-fb [b1,c]	0.68[a]	0.15	0.1 M NaClO$_4$	7	[178]
PCN-224(Ni) [b1]	0.68[a]	1	0.1 M NaClO$_4$	7	
PCN-224(Co) [b2]	0.860	2	Borate bufferedsolution	9.2	[182]
PCN-224(Co) [b2]	0.510	2	Borate-buffered solution	9.2	
MWCNT	0.860[a]	10			
Pb-TCPP [b3]	0.470	10	1.0 M KOH	14	[183]
Co-CuTCPP/rGO [b3,d]	0.396	10	1.0 M KOH	14	[184]

[a] data approximated from the cyclic voltammetry (CV) and linear sweep voltammetry (LSV) voltammogram figures

[b] scan rate 1 = 100 mV/s; 2 = 50 mV/s; 3 = 5 mV/s

[c] free base (non-metalated) porphyrin

[d] rGO = reduced graphene oxide

Author Manuscript

Author Manuscript

Author Manuscript

Author Manuscript

Table 3

Summary of ORR performance.

Catalyst	Onset Potential (E_{onset}; V vs. SHE)[a]	Peak Potential (E_{peak}; V vs. SHE)[a]	Current Density (mA/cm²)[b]	Electrolyte	pH	Refs.
PCN-222(Fe)@G-dye (50 wt%)	0.157 (0.306)	−0.765 (1.23)	−6.2	0.1 M KOH	13	[188]
FeTCPP@G-dye (50 wt%)	0.157 (0.306)	−0.765 (1.23)	−4.9			
PCN-222(Fe)@Graphene (50 wt%)	−0.065 (0.528)	−0.765 (1.23)	−3.8			
PCN-222(Fe)	−0.065 (0.528)	−0.765 (1.23)	−2.7			
PCN-222(Fe)@G-py (25 wt%)	0.495 (0.735)	0.317 (0.913)	−3.55	0.5 M H₂SO₄	0	[189]
PCN-222(Fe)@G-py (50 wt%)	0.495 (0.735)	0.315 (0.915)	−4.9			
PCN-224(Co)/MWCNT	0.375 (0.855)	0.247 (0.983)	[d]	0.5 M H₂SO₄	0	[182]
PCN-224(Co)	0.370 (0.860)	0.186 (1.044)	[d]			
PCN-223(Fe)	−0.5[c,h]	−1.1[c]	−0.7	0.1 M LiClO₄	–	[190]
PCN-223(Fe)	−0.32[c,e]	−1.1[c]	−1.2	0.1 M LiClO₄ + 0.3 M CH₃COOH		
PCN-223(Fe)	−0.49[c,f]	−1.1[c]	−1.75	0.1 M LiClO₄ + 0.3 M CCl₃COOH		
PCN-223-fb[g]	−0.63[c,h]	−1.1[c]	−0.25	0.1 M LiClO₄		
PCN-223-fb[g]	−0.5[c,h]	−1.1[c]	−0.72	0.1 M LiClO₄ + 0.3 M CH₃COOH		
PCN-223-fb[g]	−0.5[c,h]	−1.1[c]	−1	0.1 M LiClO₄ + 0.3 M CCl₃COOH		
Pt/C	1.0 (0.23)	0.750 (0.580)	−6	0.1 M HClO₄	1	[191]

[a]E_{onset} is the potential at which catalytic activity begins; E_{peak} is the potential at which the catalytic wave reaches its highest current; Overpotentials (η) are given in parentheses.

[b]The reported current density is at E_{peak}.

[c]ORR was performed in DMF, therefore overpotentials are not given.

[d]The electrode size was not reported.

[e]Measurable current was observed as early as −0.25 V vs. SHE.

[f]Measurable current was observed as early as 0 V vs. SHE.

[g]free base (non-metalated) porphyrin.

*h*Potential was estimated from CV trace.

Author Manuscript Author Manuscript Author Manuscript Author Manuscript

Table 4

Summary of CO$_2$RR MOF catalysts.

Catalyst	Overpotential (η, V)	Current density(mA/cm^2)	Faradaic Efficiency (%)	TOF(h^{-1})	Solvent^a	Refs.
MOF-525(Fe)	0.650	5.9	FE$_{CO}$ = 40 FE$_{H2}$ = 60	475	1 M TFE in MeCN	[167]
MOF-525(Fe)	0.650	2.3	FE$_{CO}$ = 54 FE$_{H2}$ = 45	64	MeCN	
Al$_2$(OH)$_2$TCPP(Co)	0.594	1	FE$_{CO}$ = 76	200	0.5 M K$_2$CO$_3$	[197]
PCN-222(Fe)/C	0.494	1.2	FE$_{CO}$ = 91	50	0.5 M KHCO$_3$	[195]
Cu$_2$(CuTCPP)	0.350	4.5	FE$_{HCOO}$ = 68.4 FE$_{CH3COO}$ = 16.8	2185	1 M H$_2$O / 0.5 MEMIMBF$_4$ in MeCN	[196]

^{a}TFE = trifluoroethanol; EMIM = 1-ethyl-3-methylimidazolium

Table 5

Performance of porphyrin MOF electrodes for nitrite sensing.

	Linear range (μM)	Sensitivity (μA/mM·cm^2)	LOD (μM)	Applied potential (V vs. SHE)	Refs.
MOF-525/GNR drop casted	100–2500	93.8	0.75	1.05	[221]
MOF-525 grown on FTO	20–800	95	2.1	1.10	[218]
Zn-TCPP(BP)	1–2000	158.1	0.26	1.04	[222]